AN ABSTRACT OF THE THESIS OF

Nilesh Araligidad for the degree of Master of Science in Atmospheric Science
presented on August 02, 2007.
Title: Buoy and Satellite Observation of Wind Induced Surface Heat Exchange in the Intraseasonal Oscillation over West Pacific and Indian Ocean

Abstract approved: ______________________________
Eric Maloney

The importance of wind-driven latent heat fluxes for supporting tropical intraseasonal precipitation variability is analyzed. Tropical intraseasonal variability in the west pacific and Indian ocean is analyzed for northern and southern hemisphere summer during 1999-2005 using satellite and buoy observations. A composite analysis of QuikSCAT ocean vector winds and TRMM precipitation for the intraseasonal oscillation (ISO) indicate that enhanced precipitation is associated with anomalous surface westerly flow over the west Pacific and the Indian oceans. Anomalous westerly flow associated with the ISO is also accompanied by enhanced wind speed over the west Pacific and Indian ocean. Enhanced wind speed during westerly phases in the west Pacific and Indian oceans suggests an increase in the wind-driven component of latent heat flux.

An analysis using TAO buoys and TRMM precipitation shows a significant correlation between intraseasonal (30-100 day) latent heat flux and TRMM precipitation in the region where enhanced precipitation occurs during the ISO westerly phase. Latent heat flux anomalies are about 20% of precipitation anomalies, a magnitude approximately sufficient as suggested by previous studies to support a

flux-driven convective instability. The correlation of QuikSCAT wind speed and TRMM precipitation was analyzed over the west Pacific and it also showed a correlation of similar magnitude as the correlation of latent heat flux and precipitation. As a sensitivity test to determine how much of the latent heat flux anomalies were wind-driven, latent heat flux anomalies were recalculated at the location of strong correlation by fixing SST, boundary layer relative humidity, and boundary layer temperature to their sixty days running averages. This sensitivity analysis shows that most of the latent heat flux anomaly is wind-driven, indicating that intraseasonal precipitation may be supported by a wind-evaporation feedback mechanism.

Wind speed and precipitation anomalies also show a significant correlation in the Indian ocean. This result suggests that if latent heat flux anomalies in the Indian ocean are primarily wind-driven, then a wind-evaporation feedback mechanism may also be supported there.

Buoy and Satellite Observation of Wind Induced Surface Heat Exchange in the Intraseasonal Oscillation over West Pacific and Indian Ocean

by

Nilesh Araligidad

A THESIS

submitted to

Oregon State University

in partial fulfillment of
the requirements for the
degree of

Master of Science

Presented August 02, 2007
Commencement June 2008

Master of Science thesis of Nilesh Araligidad presented on August 02, 2007

APPROVED:

Major Professor, representing Atmospheric Science

Dean of the College of Oceanic and Atmospheric Sciences

Dean of the Graduate School

I understand that my thesis will become part of the permanent collection of Oregon State University libraries. My signature below authorizes release of my thesis to any reader upon request.

Nilesh Araligidad, Author

ACKNOWLEDGMENT

I would like to express my deepest gratitude to my academic and research advisor, Dr. Eric D. Maloney, for his encouragement, motivation, exceptional guidance and support in helping me to complete this work. I also would like to thank him for giving me funding and opportunity to work under his able guidance. Support for this work was through the National Science Foundation under Grant ATM-0327460.

I would like to thank Chris Bretherton as discussion with him during the Frontier Lecture series have helped in the progress of this thesis. I would like to thank the faculty and my peers here at COAS department, Oregon State University for providing a wonderful learning yet competitive environment for graduate studies and for being accommodating so that I could focus on my studies. The support, patience and knowledge they showed me were invaluable. Thanks also to my fellow batch-mates who made classes and the research more enjoyable.

I wish to thank Drs. Dudley Chelton, Eric Skyllingstad, and William Warnes for examining my thesis and serving on my committee. I would like to thank my family back in India for their constant support and encouragement in my ever changing career path. I would like to thank my roommates and friends for being such supportive yet critical peers during my term as a graduate student at Oregon State University. Above all, thanks to the Almighty God for showering his blessings on me.

TABLE OF CONTENTS

TABLE OF CONTENTS (Continued)

Page

LIST OF FIGURES

LIST OF FIGURES (Continued)

LIST OF TABLES

Buoy and Satellite Observation of Wind Induced Surface Heat Exchange in the Intraseasonal Oscillation over West Pacific and Indian Ocean

1. INTRODUCTION

1.1. Background

1.1.1. Structure of the MJO

The Madden Julian Oscillation (MJO), or Intraseasonal oscillation (ISO) is the dominant mode of intraseasonal variability in tropical convection and the large-scale circulation. It consists of planetary scale (zonal wave number 1-3) perturbations in the atmospheric circulation and deep convection in the tropics, with coherent signals in many other variables (Madden and Julian 1994). The ISO propagates eastward at phase speeds of on average $5ms^{-1}$ and $10-15ms^{-1}$ west and east of the date line, respectively. The dominant periods of the ISO range between 30 and 90 days, with a strong spectral peak observed at 50-60 days. Interaction between anomalies in convective activity and the large-scale circulation is strongest in the eastern Indian and western Pacific oceans, where the oscillation reaches its maximum amplitude.

In the equatorial Indian and western Pacific oceans, an ISO event features a large-scale, eastward-moving center of strong deep convection and precipitation, with weak deep convection and precipitation regions to both its east and west. I hereafter refer to periods of strong precipitation as the "enhanced phase" of the

ISO, and periods of weak precipitation as the "suppressed phase". Precipitation anomalies are accompanied by an anomalous overturning zonal circulation, which has a first baroclinic mode structure. In the lower troposphere (850-hPa level) and near the surface, anomalously strong westerly winds exist in and to the west of the large-scale convective center, with anomalous easterly winds to the east. In the upper troposphere (above 10km or 200-hPa level), the zonal wind anomalies are of opposite sign to those in the lower troposphere.

The ISO wind anomalies displays characteristics of both a forced response and a radiating response (Hendon and Salby, 1994). The forced response appears as a coupled Rossby-Kelvin wave, similar to the Gill (1980) model response to an atmospheric heating anomaly on the equator. This Rossby-Kelvin response migrates eastward with the convective anomaly at about $5ms^{-1}$ across the eastern hemisphere. The radiating response takes the form of a Kelvin wave, which propagates eastward at about $10-15ms^{-1}$ into the western hemisphere away from the eastern hemisphere convective anomaly. The Gill model (1980) showed that the response to the west of heating is an equatorial Rossby wave, which is characterized by cyclonically rotating eddies either side of the equator in the lower troposphere, while to the east the response is the Kelvin wave. Converging low tropospheric winds of the Kelvin and Rossby waves rise in the cumulonimbus clouds of the heating region, and diverge in the upper troposphere such that flow is easterly (westerly) to the west (east) of the convective heating center.

A fundamental characteristic of the ISO is its variation in strength and latitude as a function of the seasons (Madden, 1986; Salby and Hendon, 1994). To analyze the seasonality of the ISO, Salby and Hendon (1994) used outgoing longwave (OLR) data filtered to frequencies of 35-95 days and wavenumber 1-3. A seasonal cycle of variance was then generated by averaging on individual days of the year. The ISO signal amplifies following the winter solstice and peaks near the vernal equinox at $5^o S - 10^o S$. The signal decays thereafter and migrates into northern hemisphere. A secondary peak, but weaker than the southern hemisphere peak, appears near autumnal equinox at around $10^o N$. The signal then decays and migrates into the southern hemisphere and amplifies again following the winter solstice. Salby and Hendon (1994) also examined seasonal variations at a location in Indian Ocean ($84^o E$) and found that the ISO signal peaks during both equinoxes when maximum variance is near the equator. The ISO signal over the Indian ocean amplifies prior to the onset of the Asian monsoon, when it drifts northward, and again prior to the onset of the Australian monsoon, when it drifts southward across the equator.

In the broader tropical region, ISO signals in the low-level zonal wind migrate seasonally in latitude, with peak activity located south of the equator in boreal winter and north of the equator in boreal summer (Salby and Hendon 1994). The primary peak season in SH summer is related to the Australian summer monsoon, while the secondary peak season is related to the Asian summer monsoon. During the northern hemisphere summer a) fundamental and unique characteristic of the ISO is the northward propagation of ISO convection and winds within individual ISO events (Lau and Chan 1986, Lawrence and Webster 2002). This northward propagation during boreal summer accompanies the eastward propagation of the ISO that is present throughout the year (e.g Wheeler and Hendon 2004). The seasonal migration of ISO variance in latitude is much stronger in the western Pacific Ocean than in the Indian Ocean (Zhang and Dong, 2004). Maloney and Kiehl (2002) also found that the ISO has an additional amplitude maximum over the eastern Pacific during the boreal summer, but is very weak there during the boreal winter.

1.1.2. Review of MJO theory

Although the observational description of the ISO has progressed steadily since the 1970's, a theoretical understanding of the slow eastward propagation and large-scale zonal structure of the oscillation has been lacking. The vertical structure and the eastward propagation of ISO documented by Madden and Julian stimulated early hypothesis that the MJO could be explained by Kelvin waves dynamics, since Kelvin waves also propagate eastward and have zonal wind anomalies similar in structure to the ISO, with a maximum on the equator (Lindzen 1974; Chang 1977). But it was found that ISO propagates with a much slower eastward propagating speed than the "free" Kelvin wave, which propagates eastward at a phase speed of $30 - 60ms^-1$. To account for the slow propagation speed Chang (1977) proposed that the ISO might be convectively forced Kelvin waves that are subjected to damping arising from Newtonian cooling or cumulus friction. Further, when interactions between convection and large-scale dynamics are taken into account, Kelvin wave propagation speed can be slowed. However, convectively coupled Kelvin wave phase speeds are still faster than the ISO (e.g., Hayashi and Sumi 1986; Lau and Peng 1987; Chang and Lim 1988). Also, Wheeler and Kiladis (1999) used satellite-observed outgoing longwave radiation (OLR) to show that convective variance associated with the ISO lies in a part of wavenumber-frequency symmetric OLR spectrum which is distinct from the dispersion curves of convectively coupled Kelvin waves. Kelvin waves may still be important to the ISO, however. Hendon and Salby (1996) found that the radiating western hemisphere response to the ISO is likely explained by Kelvin waves.

Based on the observational evidence that the interaction between deep moist convective activity and large-scale circulation is important in the ISO, convective activity plays a key role in theories proposed for the ISO. Such theories as related to the Kelvin wave are described above. Three additional major theories centered on the interaction of convective heating and large-scale dynamics have been proposed to explain the ISO. The first theory, wave-CISK (Conditional Instability of Second Kind) invokes an instability arising from interaction between convective heating and large-scale wave motion. The second theory proposes the importance of wind-induced surface heat exchange (WISHE), also know as wind-evaporation feedback (Emanuel, 1987; Neelin et al., 1987). The third theory suggests that an instability can arise from a friction-induced surface moisture-convergence feedback (e.g. Wang, 1988a, Maloney and Hartmann 1998).

The CISK instability mechanism hypothesizes that low-level moisture convergence and latent heat release augment each other in a positive feedback that creates an atmospheric instability at large scales. The atmosphere is assumed to be conditionally unstable to moist convective motions. CISK type instability provides the energy needed to maintain the oscillation by conversion of CAPE (Convectively Available Potential Energy) to large-scale motions. A certain amount of ambiguity exists as to whether CISK type instability can really exist. It has been observed that rather than exhibiting high levels of large-scale convective instability, lower tropospheric convective regions are actually near neutral with respect to moist adiabatic motions (Emnauel 1988; Xu and Emanuel 1989). Lim et. al (1990) and Crum and Dunkerton (1992) note that because linear wave-CISK theory predicts increasing growth with increasing wavenumber, such a flow field will eventually be overwhelmed by the smallest scales in the system. However, observations suggest that tropical intraseasonal disturbances are dominated by planetary-scale features. Many of the wave-CISK models also produce faster than observed eastward propagation. Eastward propagation appears to be slowed by changing the diabatic heating profile. When convective heating was maximized in the lower troposphere in multi-layer model (Sui and Lau, 1989), the eastward propagation was slowed. The model results of Mapes (2000) also suggest that an unstable large-scale intraseasonal mode can occur when the convective heating profile shows a significant stratiform or shallow heating component, captured by a second vertical heating mode with out-of-phase relationship between the lower and upper troposphere.

Some studies have attempted to ameliorate the instability catastrophe of wave-CISK theories by which instability collapses to the smallest scales has been treated by including the effects of surface friction on moisture convergence in the atmospheric boundary layer to produce a ”frictional-CISK” or ”frictional convergence” theory of the ISO (Wang, 1998a; Salby et al., 1994). Frictional convergence theory is different from wave-CISK theory in that the wave-induced moisture convergence alone does not result in instability (Wang, 1988a). Instead, frictional damping in the boundary layer organizes convective heating and produces a coupling between equatorial Kelvin and Rossby waves, and selects a slowly eastward moving, planetary-scale unstable mode (Wang and Rui 1990a). A key feature is that the frictional moisture convergence is ahead of precipitation in the ISO as has been observed and documented with a variety of data sets (Hendon and Salby, 1994; Maloney and Hartmann, 1998; Sperber, 2003). Maloney and Hartmann (1998) found that a significant correlation exists between surface convergence and column water vapor anomalies in the western Pacific and Indian Oceans. They showed that to the east of the enhanced convection the frictional moisture convergence fosters growth of positive water vapor anomalies which helps to slowly moisten the atmosphere to a state that is favorable for convection. The frictional convergence mechanism has been shown to be sensitive to surface drag but not to cumulus parameterization (Moskowitz and Bretherton, 2000)

Wind evaporation feedback is an instability that is driven by the wind-induced surface latent heat flux. The surface wind component of a planetary-scale, intraseasonal Kelvin mode produces evaporation anomalies that are the source of instability for the ISO in the theory of ”wind-induced surface heat exchange” (WISHE) (Emanuel(1987)) or ”wind-evaporation feedback” (EWF) (Neelin et al. (1987)). In WISHE, diabatic heating due to cumulus convection is nearly compensated by adiabatic cooling in the updrafts of cumulus clouds. According to this theory, a region of anomalous convection forces anomalous low-level easterly winds to the east and low-level westerly winds to the west. This conceptual model also assumes that the mean surface winds are easterly. With mean easterly winds, wind speed is increased to the east of anomalous convection, and decreased to the west of anomalous convection (as shown in Figure 1 (a) Model I Zhang and McPhaden 2000). Since evaporation from the oceans is strongly dependent upon wind speed, evaporation anomalies are also increased to the east of the convective region, and decreased to the west. The positive anomalies of surface latent heat fluxes to the east of the convection increases the low-level moist static energy and forces anomalous convection, which leads the wave vertical velocity and creates eastward propagation. The atmosphere is assumed to be maintained in a state of moist neutral stability unlike in wave-CISK, and convection only occurs when boundary layer moist static energy increases through surface latent heat fluxes. Such an asymmetric heat flux pattern relies on the existence of mean surface easterlies.

Observational evidence does not support the WISHE model as originally formulated. Over the Indian ocean and western Pacific where the ISO is most active the observed mean winds are westerly and not easterly near the equator. TOGA-COARE experiment observations which were conducted from November 1992 to February 1993, that included a few ISO events showed that the enhanced latent heat flux occurs in westerly wind anomalies near and to the west of ISO convection, and suppressed latent heat flux is associated with the low-level easterly anomalies (as shown in Figure 1 (b) Model II Zhang and McPhaden 2000).

Recent observational and modeling results suggest that wind-induced surface heat exchange may support ISO convection, but not in the manner originally formulated by Emanuel (1987) and Neelin et al. (1987). Jones and Weare (1996) used the International Satellite Cloud Climatology (ISCCP) and European Center for Medium-Range Weather Forecast reanalysis data to study whether low-level moisture convergence and surface latent heat flux support the ISO. Their results show that over the equatorial Indian and Pacific Oceans latent heat fluxes exhibit significant spectral peaks in the frequency band of the ISO. Significant latent heat flux spectral power was primarily caused by oscillations of the wind field, rather than by variations in the air-sea specific humidity difference. They observed that the latent heat anomalies peaked to the western side of the region of convective activity, and were suppressed to the eastern side, apposite to the relationship in the conceptual model developed by Emanuel (1987).

Hendon and Glick (1997) used Outgoing Longwave Radiation (OLR) and ECMWF analysis data to examine the relation between intraseasonal variations of convection, sea surface temperature, surface wind stress, and surface fluxes of latent heat and radiation in the warm pool of the equatorial Indian and western Pacific oceans. They found that anomalous evaporation results primarily from anomalous surface westerlies. Evaporation lagged convection by about 1-2 weeks over the Indian ocean, and 1 week or less over the west Pacific ocean.

Using TOGA COARE and ECMWF reanalysis data over a period from November 1992 to February 1993 that spanned 3 ISO events, Lau and Sui (1997) did a composite study of SST and surface flux variations associated with the ISO.

They found that the latent heat flux is lowest in the clear-sky region where the winds are weak. Latent heat flux is highest just one week after enhanced convection, since the winds associated with the ISO are strongest there. Zhang and McPhaden (1995) used moored buoy data for the time period July 1991 to June 1993, from the equatorial Pacific ($8^oN - 8^oS, 95^oW - 137^oE$) to examine the relationship between sea surface temperature (SST) and latent heat flux from the ocean. On the 30-90 days time scale they found that the latent heat flux and wind speed were mostly in phase over the western and central Pacific ocean, whereas the air-sea humidity difference was out of phase with the latent heat flux, suggesting that the latent heat flux is primarily wind driven. In the tropical eastern Pacific, data to the east of 140^oW, they found that the latent heat flux was in phase with the air-sea humidity difference and the wind speed variability was very weak thus suggesting that the latent heat flux is more controlled by anomalies in the air-sea humidity difference in the east Pacific.

Some recent modeling evidence suggest the importance of wind evaporation feedback to the ISO. Xie et al. (1993a) investigated the stability of a moist atmosphere using a model described by the linear reduced gravity equations forced by non-linear cumulus heating. They found that the atmosphere is stable and at rest to wave-CISK, but by the inclusion of wind speed dependent surface evaporation the atmosphere was destabilized. The energetics of the Evaporation Wind feedback (EWFB) and wave-CISK instability in their study showed that the wave-CISK required a small ascending and broad descending areas whereas the ascending motion in EWFB instability causes tropical convection to organize on the planetary scale and a wave-number one. Their analysis suggest that the EWFB may produce an eastward moving planetary-scale instability consistent with previous GCM experiments (Neelin et al. 1987; Namaguti and Hayashi 1991). Neelin et al. 1987 found in their GCM experiments that when the wind speed dependence was removed from the surface evaporation bulk formula, the eastward propagating wave-number one mode significantly reduced in amplitude. Whereas Namaguti and Hayashi (1991) in their experiments found that eastward propagation became invisible when the wind speed dependence of the surface evaporation was removed.

Xie et al. (1993b) examined a fully nonlinear two-Level model, in which wave-CISK and EWFB are both important in organizing tropical convection and are not mutually exclusive as in the quasi-linear model of Xie et al. (1993a). They found in their model that eastward propagating phase speed was less than the dry Kelvin phase speed but too large than the observations. The eastward propagation wave-number one appear even if the initial stratification is conditionally unstable. Wang and Li (1994) in their theoretical model used three mechanisms for the convective interaction with large-scale circulation ; wave-CISK, EWFB and convection-friction convergence. This model showed that EWFB is found to lead to instability and to enhance eastward propagation which does not necessarily require the existence of mean easterlies.

Maloney and Sobel (2004) examined the ISO in an atmospheric general circulation model (GCM) coupled to a slab ocean model(SOM). They studied model ISO sensitivity to the depth of the ocean mixed layer. The amplitude of intraseasonal precipitation anomalies was strongest in a 20m depth SOM simulation, a mixed layer of plausible depth for the west Pacific warm pool. Precipitation amplitude strongly diminished in a 2m depth SOM simulation. The small ocean heat capacity of the 2m run strongly diminished surface evaporation anomalies in the model.A simulation was also performed were the wind-evaporation or WISHE feedback was explicitly suppressed (No-WISHE) by fixing the SST and setting the latent heat fluxes to their climatological seasonal cycle. The amplitude of intraseasonal precipitation variations in the No-WISHE simulation was more similar to the 2m SOM simulation than those of the other SOM simulation and the control simulation, indicating that WISHE was important to the intraseasonal variability in this model.

Wind-induced heat exchange also appears to be important for supporting intraseasonal convection in other parts of the tropics. Maloney and Esbensen (2003) showed using reanalysis fields that ISO surface southwesterly anomalies accompany enhanced latent heat fluxes and convection in the east Pacific warm pool during boreal summer, suggesting that wind-evaporation feedback may support east Pacific convection. Strong westerly surface wind anomalies in association with mean westerly surface winds over the east Pacific warm pool lead to enhanced westerly flow during convectively active periods of an ISO life cycle. These westerly anomalies are accompanied by positive latent heat flux anomalies which may then be communicated to convective regions to the east by westerly surface flow. Suppressed precipitation and negative latent heat flux anomalies accompanied by surface easterly intraseasonal wind anomalies added to westerly seasonal cycle winds.

Maloney and Esbensen (2005) used a general circulation model that produces realistic east Pacific intraseasonal variability to examine the influence of wind-evaporation feedback on the ISO. When the latent heat fluxes were prescribed by their climatological seasonal cycle, intraseasonal precipitation variations of amplitude significantly lower than observations were produced. Variations in wind speed dominated variations in latent heat flux, whereas air-sea specific humidity deficit variations had negligible impact on surface flux anomalies. Diabatic heating anomalies associated with convection acted to strengthen large-scale circulation anomalies thereby strengthening surface heat flux anomalies. The results of Maloney and Esbensen (2005) thus suggested that intraseasonal precipitation variations are supported by a wind-evaporation feedback mechanism.

Maloney and Esbensen (2007) using buoy and satellite observations of boreal summer intraseasonal variability in the tropical northeast Pacific found a significant positive covariance between MJO precipitation and latent heat flux. An enhancement of latent heat flux occurred in association with MJO surface westerly wind anomalies and enhanced precipitation. Periods of anomalous ISO westerly flow are generally accompanied by enhanced wind speed, while periods of anomalous easterlies are associated with suppressed wind speed. During the westerly phase, south westerly intraseasonal vector wind anomalies combined with climatological southwesterly flow account for the bulk of wind speed enhancement in the warm pool, with much weaker contribution from enhanced eddy variance. Suppression of wind speed during the ISO easterly phase has strong contributions from both northeasterly intraseasonal vector wind anomalies added to the mean south westerly flow and suppression of eddy activity on timescales of less than 20 days.

Latent heat flux is not the only possible energy source to support intraseasonal convection. Cloud-radiation feedbacks could also be important in the maintenance of the ISO oscillation. Lin and Mapes (2004) used top of the atmosphere (TOA) and surface radiative flux measurements during the Atmospheric Radiation Measurement (ARM) and TOGA COARE experiments, supplemented by long-term TOA flux measurement from ERBE and AVHRR, to estimate intraseasonal variations of the atmospheric radiation budget. They found that the column-integrated radiative heating lags the column-integrated convective heating by less than 5 days and enhances the convective heating by about 10%-15%. They found that the dominant contribution to the atmospheric radiative heating is primarily due to longwave radiation, as clouds and small contributions from water vapor reduce the TOA outgoing longwave radiation (OLR) during ISO convective events.

Using observational data, and the assumption of a deep convective heating profile Yu et al. (1998) found that the gross moist stability M is positive but smaller than the typical static stability values M_s in the tropical convective region. The gross moist stability is the net export of moist static energy per unit of vertical mass flux in deep convective regions. The gross moisture stratification M_q which is the instability driven by lower-level moisture convergence causes the gross moist stability M to be less positive than the static stability values M_s. They estimated the typical values of M and M_q in the tropics are roughly 500 and 2500J kg^{-1}, respectively. Lee et al (2001) used the assumptions and results of Yu et al. (1998) to estimate that a 20% enhancement of column-integrated diabatic heating by longwave cloud radiative heating was necessary for the atmosphere to reach radiative-convective instability, which is greater than the Lin and Mapes (2004) observed estimates, suggesting that cloud feedbacks alone are not sufficient to foster instability. Lee et al (2001) used an Atmospheric General circulation model (AGCM) to study the influence of cloud-radiation interaction on the tropical ISO simulation. They carried out two simplified aqua planet experiments using the AGCM, one using fully interactive clouds and radiation and the other using fixed radiation in which a zonal mean radiative cooling rate was prescribed. Under the fixed radiation case eastward wave propagation with zonal wave-number 1-2 is simulated that resembles the excitation of equatorial moist Kelvin waves. When cloud-radiation interaction is included eastward propagation is inhibited significantly by the excitations of small-scale disturbances, caused by strong positive radiative feedbacks induced by the cumulus generated anvil clouds, strong complementary interactions occur between cloud-induced radiation anomalies and the large-scale circulation. Westward movement was gradually reduced and the waves again propagated eastward with zonal wavenumber 1 structure and about 30 day period when the precipitation time scale was reduced, effectively weakening the cloud-radiative feedback. Reducing the precipitation timescale generates raindrops more quickly and removes cloud droplets, thus reducing cloud radiative feedbacks. Reduction of the precipitation time-scale weakens the positive feedback of anvil cloud on longwave radiation and Kelvin wave CISK operates to show planetary scale wave propagation. One of the shortcomings of reducing the precipitation time-scale was that there was considerable discrepancy of the radiation budget simulated at the top of atmosphere relative to the standard simulation and observations.

Bony and Emanuel (2005) used a simple linear model of a nonrotating two-dimensional tropical atmosphere with constant background wind and surface temperature to study how atmospheric moisture interacts with radiation and convection to modulate intraseasonal variability. The primary effect of moisture-radiation feedbacks is to reduce the phase speed of large-scale tropical disturbances by cooling the atmosphere less efficiently during the convectively enhanced phase than during periods of large-scale subsidence. The planetary waves predicted by the linear model in the presence of significant moist radiative feedbacks are characterized by an approximately constant frequency of 50-60 days, the approximate timescale of the ISO. The drawback of the linear model used in Bony and Emanuel (2005) is that it neglects the shading effect of clouds on the surface radiation budget, and neglects convective downdrafts that affect surface evaporative cooling through their modulation of the subcloud-layer moist entropy.

Using a numerical model of intermediate complexity, Raymond (2001) found that an instability dependent on cloud-radiation interaction produced a planetary-scale tropical mode of wavenumber one that moved eastward at about $5ms^{-1}$. The important structural components of this mode are large, low-level cyclonic gyres on one or both sides of the equator coupled to a strong low-level westerly jet near the equator with intense precipitation at the eastern end of the jet. When an equatorial warm pool is imposed upon a zonally symmetric SST distribution, convective outbreaks periodically develop over the warm pool, move eastward, and dissipate once the edge of the warm pool is reached, similar to the observed ISO. Model precipitation lags enhanced surface fluxes by several days, since the model has a smooth inverse relationship between tropospheric saturation deficit and precipitation rate.

As described by Zhang (2005), recent observational work has been able to provide a much better characterization of the ISO's vertical structure, air-sea coupling, and interaction with higher frequency weather events. However, many gaps in our understanding remain. For example, much of the current analysis of the vertical structure of the ISO is largely based on global model reanalysis products, the results of which are highly dependent on the parameterization assumptions of the analysis models. While realistic ISOs can be produced by idealized models that can be specially formulated to isolate the roles of specific mechanisms, GCMs with more advanced treatment of physical processes have a difficult time in simulating the ISO (e.g. Zhang 2005). Many new ideas and hypotheses have been proposed to explain the ISO, but these hypotheses have not been able to quantitatively explain why GCMs cannot simulate the ISO, in addition to not being able to predict the selection of the observed time and space scales and phase speed (Zhang 2005).

We can improve our GCM simulations of the intraseasonal variability through improved observational characterizations of the ISO. The work conducted here is an observational study that examines the viability of wind-evaporation feedback as a means for supporting ISO convection. This study examines the relationship between intraseasonal Tropical Rainfall Measuring Mission (TRMM) precipitation and Tropical Ocean-Global Atmosphere (TOGA) Tropical Atmosphere Ocean (TAO) buoy latent heat fluxes in the west Pacific during 1998-2005. A comparison with TRMM precipitation allows the relative magnitudes of intraseasonal precipitation and latent heat flux anomalies to be determined that would suggest the importance of wind-evaporation feedback to the ISO moist static energy budget. Previous studies that have examined the relationship of surface evaporation to ISO convection have relied in-part or in-whole on model analyses to determine fluxes (e.g. Jones and Weare 1996, Shinoda et al. 1998, Sperber 2003), or on in-situ measurements with relatively short data records (e.g. Lau and Sui 1997). The work of Zhang (1996) and Zhang and McPhaden (2000) is the most similar to the present study in which they use data from the TAO buoy array to examine the evolution of the surface heat budget during ISO events. However, Zhang (1996) used a limited three year period (1991-1994) to examine buoy latent fluxes and their relationship to ISO high cloud cover, and Zhang and McPhaden (2000, their Figure 2) concentrated on buoy fluxes within two degrees of the equator. Use of high cloud clover as a proxy for precipitation was noted by Zhang (1996) as a weakness of his study.

This study is also new in that it uses the Quick Scatterometer (QuikSCAT) ocean vector wind product during 1999-2005 to determine how wind speed variations are related to ISO precipitation in the west Pacific and Indian Ocean. This comparison is enlightening because latent heat flux anomalies in the west Pacific during ISO events will be shown to be primarily wind-driven

1.2. Why studying the ISO is important

The intraseasonal oscillation (ISO) affects a wide range of tropical weather such as the onset and breaks of the Indian and Australian summer monsoons (Yasunari 1979, Hendon and Liebmann 1990) and the formation of tropical cyclones (Liebmann et al 1994). It also is associated with strong teleconnections to the extra-tropics (e.g. Lau and Philips 1986, Winkler et al. 2001) that lead to significant impacts on extra-tropical weather (e.g. Higgins and Mo 1997, Higgins et al. 2000). The ISO also exhibits interactions with longer timescale phenomena. For example, the ISO is observed to trigger or terminate some El Nino events by forcing oceanic Kelvin waves (e.g. Kesseler et al. 1995, Takayabu et al. 1999, Bergman et al. 2001). Therefore, the ISO is important for both extended-range weather forecasting and long term climate prediction.

The processes that regulate interactions between convection and the large-scale circulation associated with the ISO are not well understood. Further, climate models have difficulty simulating the ISO and other processes related to interactions between convection and the large-scale interaction (e.g. Slingo et al. 1996). If we can understand how convection interact in the ISO, then we may be able to improve our model representations of convectively coupled processes on a variety of timescales. The observational studies done in tropical east Pacific (Maloney and Esbensen 2007) and modeling studies done in the tropical east (Maloney and Esbensen 2005)and west Pacific (e.g. Maloney and Sobel 2004) suggest that wind-evaporation feedback, of which the large-scale circulation is an integral part, plays a role in the enhancement of convection in the intraseasonal oscillation. The goal of this study is to examine the co-variability of wind speed, latent heat flux, and precipitation anomalies over the west Pacific and Indian Oceans associated with the

ISO using buoy and satellite observations to intimate whether a wind-evaporation feedback mechanism supports intraseasonal precipitation anomalies.

1.3. Overview of study

This thesis is a study to analyze the wind-evaporation feedback mechanism over the west Pacific and Indian oceans using the satellite data and buoy observations

Chapter two deals with the data products and the methods used in this study. Chapter three begins with an analysis of the mean wind and precipitation in the west Pacific, and the spatial distribution of intraseasonal precipitation variance. Correlation of 30-100 day wind speed and precipitation is analyzed. Correlation of the latent heat flux and precipitation anomalies associated with ISO is examined, and a sensitivity analysis is conducted that determines the relative importance of wind speed anomalies to latent heat flux anomalies. The importance of latent heat flux anomalies to the moist static energy budget of intraseasonal convection is analyzed. Composite analysis using the precipitation, wind speed and the vector winds associated with the ISO in the west Pacific is carried out for both northern hemisphere and southern hemisphere summer. Buoy data are used to examine the evolution of composite latent heat flux anomalies during ISO events, and the dependence of these anomalies on anomalies in wind speed and air-sea humidity differences. Similar satellite-based analysis are conducted in chapter 4 for the Indian ocean as in chapter 3 for the west Pacific. Chapter five presents conclusions.

2. DATA AND METHODOLOGY

2.1. Datasets

2.1.1. TAO Buoy data

The Tropical Atmosphere Ocean (TAO) buoy array data is used to compute latent heat flux . The TAO buoy array (renamed the TAO/TRITON array on 1 January 2000) consists of 70 moored buoys deployed in a regular array across the equatorial Pacific ocean as a part of the Tropical Ocean Global Atmosphere Program (Hayes et al. 1991; McPhaden 1995). The oceanographic and meteorological data are telemetered to the shore in real time via the Argos satellite system. Figure 2.1 shows the array of TAO buoys in the equatorial Pacific ocean. They span the region between 136E to 90W and 8N to 8S. The filled circles seen in the Figure 2.1 indicate the buoy locations used in this study, encompassing the west Pacific where intraseasonal variance maximizes.

Daily average data of relative humidity, air temperature, wind speed and one meter depth sea surface temperature were downloaded from the TAO/TRITON data delivery website (http://www.pmel.noaa.gov). At each buoy location, missing data within data gaps of less than or equal to ten consecutive days are filled by linear interpolation. Since we are interested in the intraseasonal oscillation, interpolating missing data in this manner only minimally impacts information within the time scale of 30-90 days.

Surface latent heat fluxes are calculated using version 3.0 of the Coupled Ocean-Atmosphere Response Experiment (COARE) flux bulk algorithm (Fairall et al. 2003). The surface latent heat flux is estimated from the bulk aerodynamic formulae relating the turbulent flux of water vapor just above the sea surface to

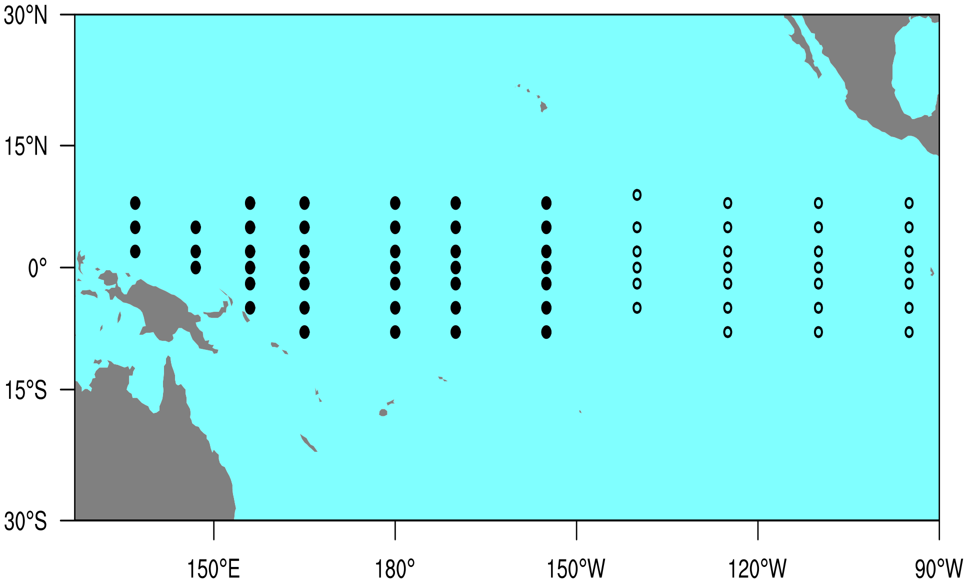

FIGURE 2.1. *TAO buoy array in the Pacific ocean.*

locally averaged values of sea surface temperature, wind speed, air temperature, and humidity in the surface boundary layer.

$$LH = \rho C_q(..., z_u, z_q)U(z_u)[q_{sfc} - q(z_q)] \tag{2.1}$$

where ρ is the air density, C_q is the transfer coefficient and is dependent on sea state, atmospheric surface boundary layer stability and the observation heights z_u, z_q above the surface. $U(z_u)$ is the wind speed at the observation height z_u. q_{sfc} and $q(z_q)$ are the specific humidities at the surface and at the observation height z_q respectively. The wind speed $U(z_u)$ is composed of a vector part (u and v components) and a gustiness part (U_g) to account for subgrid-scale variability. The COARE algorithm incorporates submodels that represent the millimeter-scale cool skin near the interface and the diurnal warm layer in the upper few meters of the ocean. The cool skin is accounted for since the true interface temperature is often several tenths ^oC cooler than the bulk water temperature near the surface. Further, warm layers can form in light wind and sunny conditions where shortwave radiation may warm the upper few meters of the ocean by $1^o - 3^oC$ relative to the deeper ocean. Since we don't have shortwave and longwave radiometer data available for most of the buoy locations for the period 1998-2005, we do not include cool skin and warm layer calculations in our estimates of latent heat flux. Maloney and Esbensen (2007) did a sensitivity test in the east Pacific to determine whether exclusion of the cool skin/warm layer calculation altered their estimates of intraseasonal flux variability, and found very little sensitivity.

2.1.2. QuikSCAT ocean vector winds

The National Aeronautic and Space Adminstration (NASA) Quik Scatterometer (QuikSCAT) satellite was launched in June 1999. The SeaWinds Scatterometer on QuikSCAT retrieves ocean surface wind stress from the ocean surface using the backscatter from multiple azimuth and incidence angles (Chelton and Frelich 2005). The SeaWinds scatterometer operates by transmitting radio frequency waves pulses to the ocean surface, and measures the intensity of the backscattered signal. A rough ocean surface returns a stronger signal, because the surface reflects more of the radar energy back towards the scatterometer antenna, than for a smooth ocean surface. The ocean surface roughness is highly correlated with the near surface wind speed and direction. Surface wind estimates are provided as the "equivalent neutral stability wind vector", the wind vector that would produce the observed wind stress if the atmospheric boundary layer were neutrally stratified.

For this study QuikSCAT vector winds were downloaded on a $0.25^o \times 0.25^o$ grid in daily ascending and descending swaths from Remote Sensing Systems of

Santa Rosa, California (http://www.remss.com) for the period 1999-2005. Because rain contamination of the backscatter signal can occur, we label QuikSCAT data as missing when radiometer data indicates that it is raining within, or adjacent to, the $0.25^o \times 0.25^o$ scatterometer grid cell. The scatterometer data was later averaged to a $1^o \times 1^o$ grid size and then linearly interpolated in time to fill any remaining gaps.

2.1.3. TRMM data

To improve the knowledge of tropical rainfall processes and climatology a joint National Aeronautics and Space Administration (NASA) / Japan Aerospace Exploration Agency (JAXA) research mission launched the Tropical Rainfall Measuring Mission (TRMM) (Kummerow et al., 2000;Adler et al., 2003). Its primary mission is to measure precipitation in the tropics ($\pm 35^o$), especially over the oceans, where surface observations are scarce. The principal precipitation measuring instruments on the satellite are TRMM Microwave Imager (TMI), Precipitation Radar (PR) and Visible and Infrared Scanner (VIRS).

In this study we use the daily averaged precipitation fields from the TMI Level 3B-42 version 6 product that were downloaded on a $0.25^o \times 0.25^o$ grid from the Goddard Space flight center distributed archive system (accessed from http://trmm.gsfc.nasa.gov) during the period 1998-2005. The $0.25^o \times 0.25^o$ grid data were then averaged to $1^o \times 1^o$ grid. The primary precipitation retrievals are based on emission of microwave radiation from raindrops, which appear warm against a cold ocean background. The TMI measures the volume-integrated emission by rain within the instrument's field of view, from which a surface precipitation rate can be inferred. The TMI is less effective over land surfaces due to inhomogeneity in the surface emissivity. Because of its low altitude and relatively narrow swath (compared to polar-orbiting sun-synchronous satellites), the TMI requires between 1 and 2 days to provide complete coverage of the tropical region. Three-hourly TRMM 3B42 precipitation estimates are derived in a multistage process that combines TMI precipitation retrievals with IR measurements from geostationary satellites.

The 3B-42 precipitation estimates are produced in several stages. First the TMI microwave estimates are calibrated and combined, and high temporal resolution infrared precipitation estimates from geostationary satellites are created by calibrating with the microwave precipitation. To produce 3-hourly data, the microwave and IR estimates are combined by using the microwave estimates where available, and then filling the other grid cells with IR derived data. Rain gauge data are then used where available to do a final scaling of precipitation estimates. Because we are interested in the relative magnitude of surface latent heat flux anomalies to precipitation from a moist static energy budget perspective, the accuracy of the TRMM precipitation anomalies is important. Intraseasonal precipitation anomalies with the TRMM 3B-42 product are though to be accurate to within 10% (Christian Kummerow, Personal communication 2007), thus providing confidence that the relative amplitudes of latent heat flux to precipitation anomalies. I present below are realistic quantitative estimates of the impact of surface flux forcing to the energy budget.

2.2. Methodology

2.2.1. Compositing technique

The ISO index constructed by Maloney and Kiehl (2002) is used in this study. The index used for compositing was constructed using the 30-90 day band-pass filtered NCEP-NCAR (National Center for Environment Prediction - National Center for Atmospheric Research) Reanalysis 1 850-mb daily zonal winds during 1979-2005. The 850-mb zonal wind was averaged from 5N-5S every 2.5 degrees of longitude around the equator. EOF analysis was then conducted on the equatorially averaged zonal wind field which contains data across all seasons. The two leading EOFs that explain a total of 59% of the intraseasonal equatorial zonal wind variance are shown in Figure 2.2 The principal components (PC's) of these leading EOF's are correlated at 0.6 at a lag of 12 days, with PC2 lagging PC1. An ISO time series is defined by adding PC1 to the value of PC2 twelve days later. As a check on the sensitivity of ISO time series to the data analysis product used, Maloney et al. (2007) also constructed the ISO time series using the ECMWF ERA-40 (European Center for Medium-range Weather Forecast) reanalysis dataset. The ECMWF ERA-40 reanalysis-based ISO time series was virtually identical to that obtained using NCEP Reanalysis 1. It should be noted that complex empirical orthogonal function analysis can also be used to derive an ISO index. We primarily use the EOF-based ISO index here to derive significant ISO events. For this purpose, CEOF produces identical results to the EOF based-index used here. However, CEOF better captures the propagation characteristics of eastward propagating ISO variability since it represents such variability within a single complex mode. CEOF analysis will be used in future work to better characterize the dynamics and propagation characteristics of the ISO across the tropics.

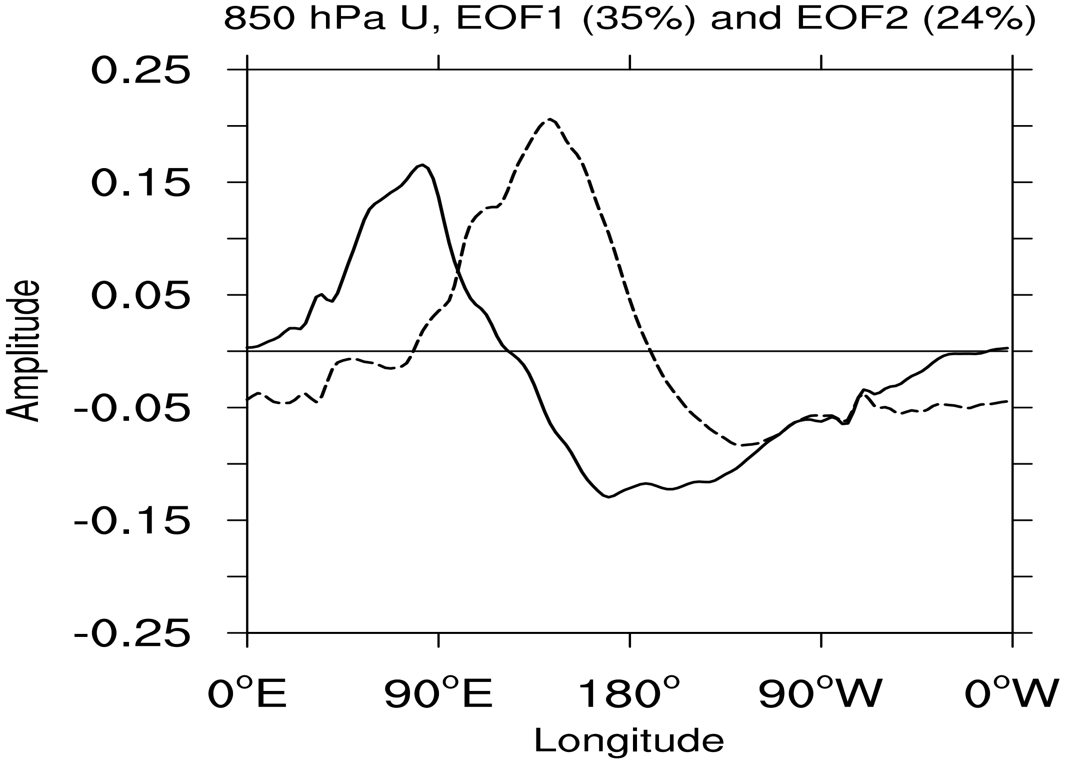

FIGURE 2.2. *EOF1 and EOF2 of the equatorial averaged ($5^oN - 5^oS$) 850hPa zonal wind as a function of longitude. Magnitudes were normalized in the computation of the EOFs. (Figure Courtesy Dr. Eric Maloney)*

The time variation of the index generally resembles an oscillating pattern much like a sinusoidally varying function (see figure 2.3). Key events were isolated by selecting index maxima of amplitude greater than one standard deviation from zero. It was ensured that each event consisted of a maximum straddled by two minima with magnitude less than zero. A total of 37 ISO events were isolated during all seasons of 1999-2005 using the above selection criterion. Twenty one of these events occurred during the northern hemisphere summer, and 16 events occurred during the southern hemisphere summer. Once the events were isolated, each event was broken into nine different phases for the purpose of compositing. The time in each event at which the index had maximum peak amplitude was

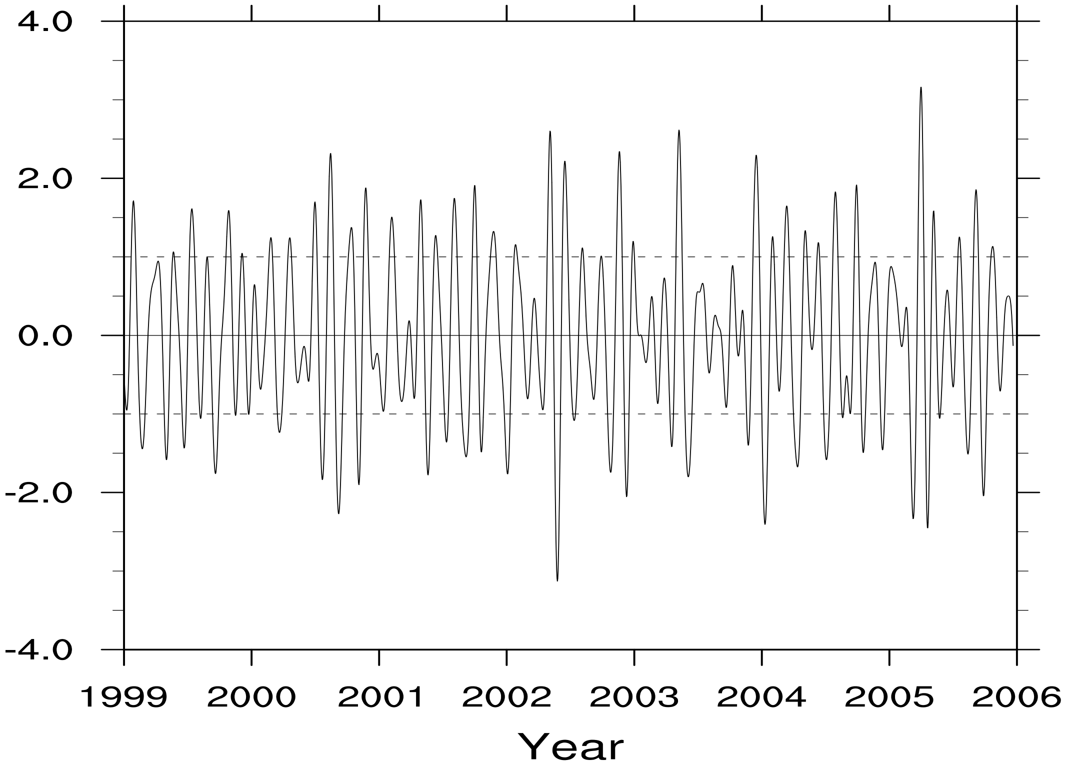

FIGURE 2.3. *MJO index time series*

designated as phase 5. The minima in each event before and after phase 5 were assigned phase 1 and phase 9, respectively . The zero increasing and zero decreasing points in each event were assigned phase 3 and phase 7, respectively. Phase 2, 4, 6, and 8 were placed equidistant in time between phases 1, 3, 5, 7, and 9. Phases were then averaged over the 21 events for the northern hemisphere summer and 16 events for the southern hemisphere summer to produce composite events consisting of 9 phases.

2.2.2. Wind speed decomposition

One interest of this study is the impact of high frequency transient activity, such as tropical cyclones and easterly waves, on wind speed at intraseasonal timescales. For example, Maloney and Dickinson (2003) showed that the ISO is associated with strong variations in eddy kinetic energy in the western north Pacific during boreal summer. Synoptic eddies with timescales less than 20 days were enhanced during the ISO westerly phase, and suppressed during the easterly phase. In presence of such fluctuations, due to the non-linear calculation of wind speed from vector wind components, eddy vector wind anomalies would be expected to have some non-zero impact on anomalous wind speed in the 30-100 day band, even though the timescales of the eddies themselves are less than this frequency band.

Intraseasonal wind speed anomalies are thus decomposed into a portion due to intraseasonal vector winds and a portion to which higher frequency fluctuations in eddy wind components have a contribution. This method is similar to that used in Maloney and Esbensen (2007). Three distinct calculations were performed on the daily averaged wind components from QuikSCAT : 1) The total intraseasonal wind speed anomaly was derived by applying a 30-100 day bandpass filter to the magnitude of the daily averaged wind vector. 2) Intraseasonal wind speed anomalies due solely to ISO vector wind anomalies are derived. To accomplish this a low-pass filter is applied to the daily average wind components to retain periods of greater than 20 days, effectively removing eddy variability. A 30-100 day bandpass filter is then applied to the magnitude of these filtered vector components. 3) the difference between wind speed anomalies 1) and 2) is computed. This third calculation indicates the portion of the ISO wind speed anomaly to which anomalies in eddy variance less than 20 days provide some contribution.

2.2.3. Bandpass filtering

Unless otherwise stated, intraseasonal wind speed anomalies are isolated by applying a linear non-recursive digital filter with half power points at 30 and 100 days (not shown).The frequency response function of the filter we use retains nearly full power at 40-50 day timescales, the dominant period band associated with the ISO as documented in observations (e.g Madden and Julian 1971)

The 30 day low pass filter has 29 weights and the 100 day high pass filter has 60 weights. In certain circumstances, 10 and 20 day low pass filters are used that are constructed using 19 filter weights.

3. WEST PACIFIC ANALYSIS

The role of wind induced surface heat exchange (WISHE) for supporting ISO convection will be examined over the west Pacific. In this section I will discuss the importance of WISHE to intraseasonal convection over the west Pacific using the TAO buoys and satellite data. Since no TAO buoy data is available for the Indian Ocean, I analyze only satellite data on section 4, to provide an indication of how intraseasonal wind speed varies with intraseasonal precipitation. Such an analysis provides a estimate of how wind-induced portions of the surface flux relate to precipitation.

3.1. 30-100 day Precipitation variance

Figure 3.1 shows TRMM intraseasonal precipitation variance (shading) and mean precipitation (contours), overlayed with mean QuikSCAT surface wind vectors for the Northern Hemisphere (NH) summer (May, June, July, August, September, and October) and Southern Hemisphere (SH) summer (November, December, January, February, March and April) in the west Pacific Ocean. During the NH summer (Figure 3.1) precipitation variance is high in regions of high mean precipitation and weak mean westerly flow with the peak variance occurring to the west of 155^oE and north of 5^oN. The mean winds have an easterly component to the east of 155^oE, with meridional convergence into the Inter Tropical Convergence Zone (ITCZ) that is centered near 7^oN. The mean winds are south easterly to the south of 8^oS. To the west of 155^oE the mean winds are generally south westerly in the NH and south easterly in the SH.

During the SH summer (Figure 3.1) the ITCZ shifts slightly south and is seen to be centered at 5^oN. The mean winds to the north of ITCZ are north

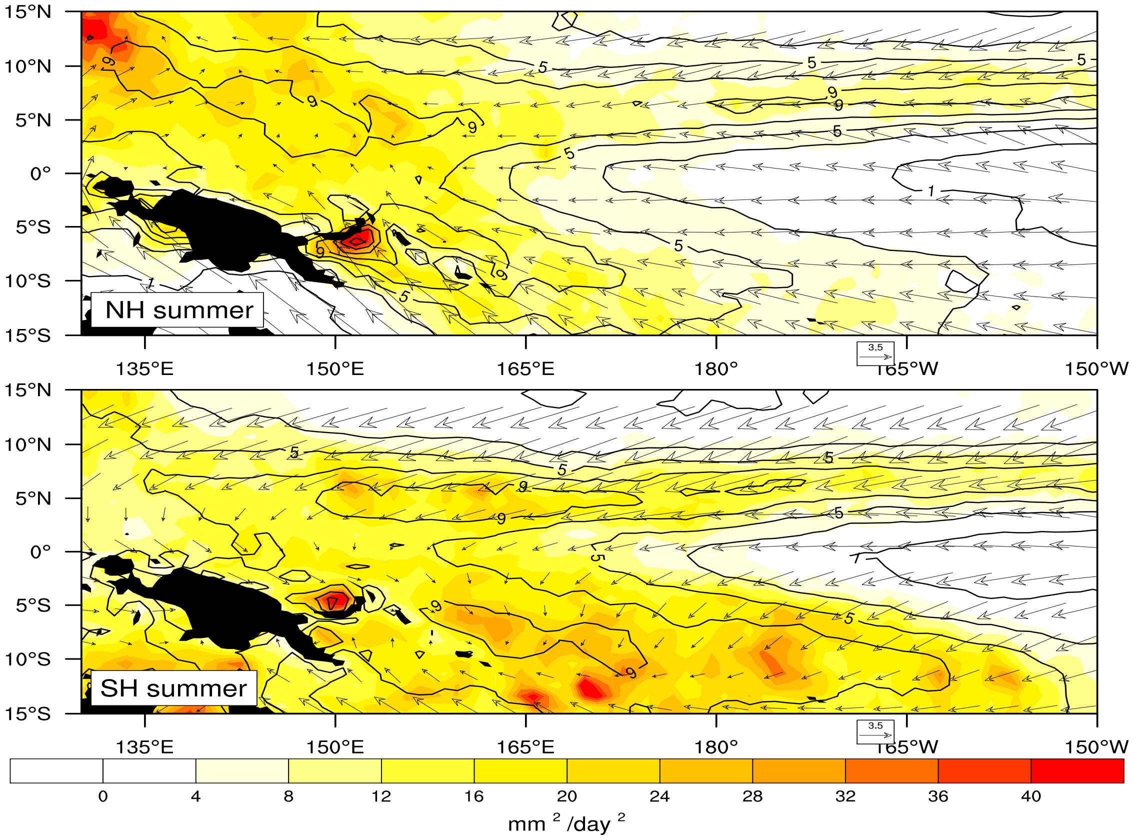

FIGURE 3.1. *Precipitation variance ($mm^2 day^{-2}$ filled contour) and mean precipitation ($mmday^{-1}$ line contour) for Northern hemisphere(NH) summer and Southern hemisphere (SH) summer. Wind vectors are the mean QuikSCAT wind.*

easterly and to the south, between the ITCZ and the equator they generally are easterly. To the west of $165^o E$, from the equator to $10^o S$ the mean winds are north westerly, with easterly winds to the south of $10^o S$. Weak north westerly mean winds prevail near and to the west of the region of peak mean precipitation and high values of precipitation variance. SH summer mean precipitation shows a second maximum along $5^o N$ in the ITCZ where we also observe high values of precipitation variance. However, overall precipitation variance during SH summer is highest in the SH between $5^o S$ and $15^o S$.

3.2. 30-100 day Correlation of wind speed and precipitation

The correlation of wind speed and precipitation can suggest whether the wind-induced component of latent heat flux anomalies support intraseasonal convection. 30-100 day QuikSCAT wind speed anomalies and TRMM precipitation anomalies show a significant positive correlation (figure3.2 a) over the region of enhanced precipitation variance shown in figure 3.1. Stippling shows regions where the correlation coefficient are significantly different from zero at 90% confidence level using the t-statistic. Since the mean period of ISO is 40 days, I conservatively use N/40 as the number of degrees of freedom, where N represent the number of days of data at a particular location. It will also be shown below that these are regions of strong precipitation anomalies during composite ISO events.

Wind speed used in the above correlation is the wind speed calculated from in-swath satellite wind components on a $0.25^o \times 0.25^o$ grid and is here after referred to as scalar wind speed. This scalar wind speed is then averaged to a $1^o \times 1^o$ grid for comparison to precipitation. Vector wind speed was also calculated (Figure 3.2 b). Average wind vectors are determined for the $1^o \times 1^o$ grid, and then the magnitude of the resulting wind vector was determined. This magnitude will be referred to as the vector wind speed. Computing a vector average wind minimizes a couple of effects. First, it reduces the effects of gustiness that accompanies mesoscale convective systems in the tropics (discussed below). Second, it minimizes the noisiness of wind retrievals from QuikSCAT that may be most acute in the $0.25^o \times 0.25^o$ grid. The relative contributions of these two effects cannot be easily separated. I note below that the relationship of buoy fluxes to precipitation more closely resembles that when using the QuikSCAT vector wind speed than the scalar wind speed, however.

The correlation of the scalar wind speed and precipitation is higher than the correlation of the vector wind speed and precipitation. During both NH summer and SH summer the correlation of scalar wind speed and precipitation is 0.7 over the region of enhanced precipitation variance. The correlation of vector wind speed and precipitation is around 0.6 during the NH summer. During the SH summer the correlation of vector wind speed and precipitation has a correlation of 0.7, but the correlation of 0.6 is over most of the region of enhanced precipitation variance.

If we average the vector wind components over a $2.5^o \times 2.5^o$ grid before calculating the vector wind speed, the correlation decreases to 0.2 during the NH summer and 0.3 during the SH summer (Figure 3.3). This may suggest that mesoscale gustiness and other high wave-number spatial features contribute to the increase in positive correlation of wind speed and precipitation anomalies. Mesoscale atmospheric motions can induce horizontal wind variability that increases the wind speed. Mesoscale precipitating systems in the tropics generate local circulations on the scale of 100 km and less that increase the wind speed (Redelsberger et al. 2000). Much of the regulation of surface winds is due to downdrafts associated with such convective systems that bring cold,dry and gusty air to the sea surface that can enhance the surface fluxes. Back and Bretherton (2005) did a sensitivity study with QuickSCAT mean vector winds and found that the gustiness effect on the wind speed is diminished when averaged over $2.5^o \times 2.5^o$. They did not explicitly examine the intraseasonal band, however. The amplitudes of the Figure 3.3 correlation with precipitation are similar to those derived when latent heat flux is computed using the three day running mean vector wind speed (see Figure 3.5),

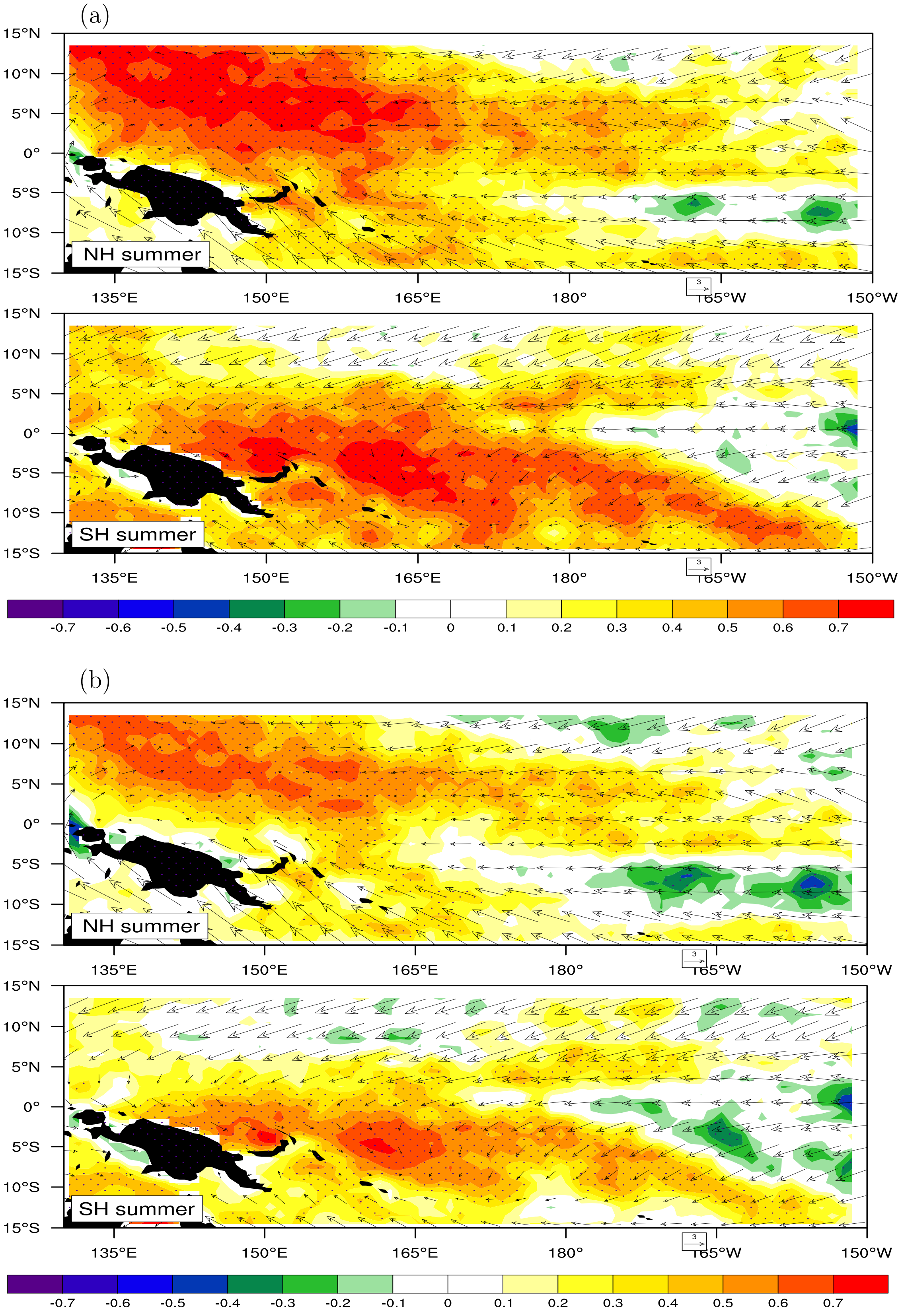

FIGURE 3.2. *Correlation of wind speed and Precipitation a) Scalar wind speed b) Vector wind speed. Stippling shows region were the correlation are different from zero at 90% confidence interval. Wind vectors are the mean QuikSCAT wind.*

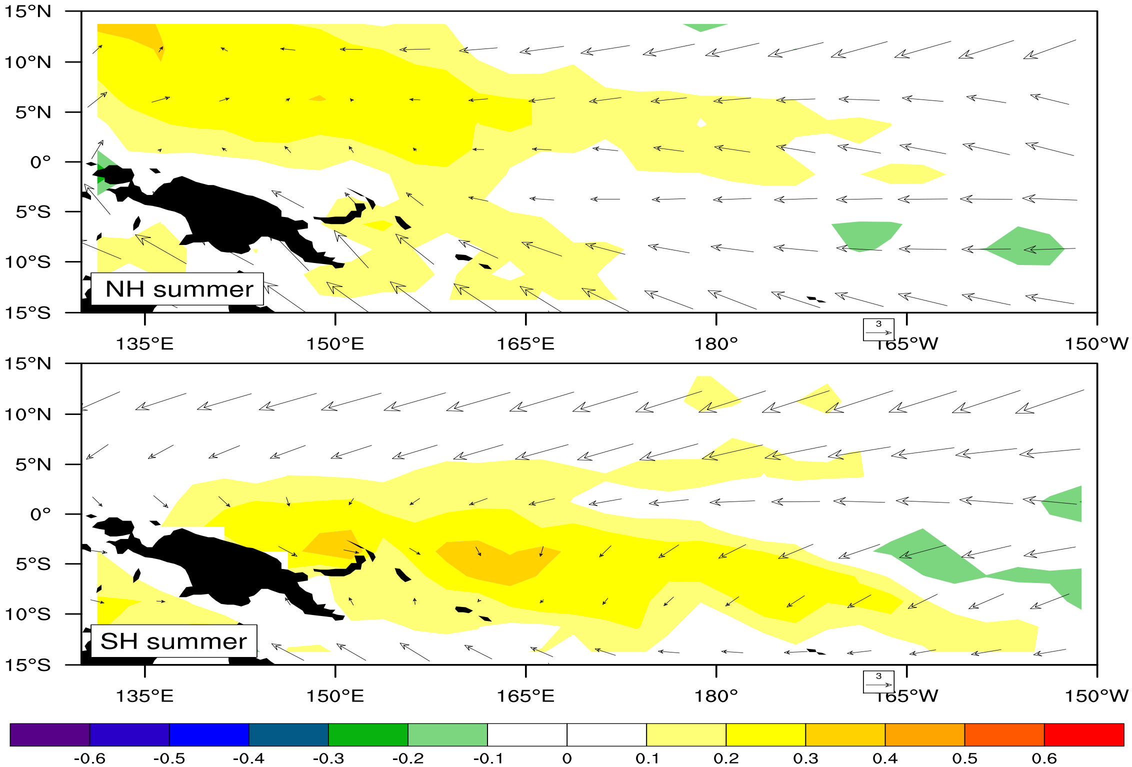

FIGURE 3.3. *Correlation of vector wind speed (computed using 2.5 grid averaged vector winds) and precipitation. Wind vectors are the mean QuikSCAT wind.*

and thus suggest that gustiness may support intraseasonal convection in the west Pacific.

3.3. Correlation of Latent heat flux anomalies and Precipitation anomalies

As discussed above, QuikSCAT fields can only be used to determine where wind speed anomalies would enhance the wind-driven part of the latent heat flux, and give no information on the actual latent heat flux itself. The TAO buoys provide sea surface temperature, atmospheric temperature, humidity, and wind speed measurements that can be used to compute surface heat fluxes in total. I use TAO buoy fields here to examine intraseasonal surface heat flux anomalies. Most importantly, these buoy fluxes will be used to derive the relative role of surface heat flux in the moist static energy budget of the tropical atmosphere during intraseasonal convective events.

Fig 2.1 shows the location of the buoys arrays in the Pacific for the period 1999-2005. The location of filled circles are the buoy locations used in this study, which cover the tropical west Pacific region. Latent heat flux was calculated using the COARE bulk flux algorithm (Fairall et al. 2003), and then filtered using the 30-100 band pass filter. TRMM precipitation data were interpolated using bilinear interpolation to the specific buoy location. Precipitation anomalies were filtered using a 30-100 day band pass filter and then converted to an equivalent energy flux in Wm^{-2}. The precipitation rate is multiplied by the latent heat of condensation and density of water (a factor of 28.935) to convert to an equivalent energy flux. Such a unit conversion will be useful when examining the linear regression coefficients shown below.

Figure3.4 (a) shows the correlation coefficients between intraseasonal precipitation and latent heat flux for the west Pacific buoy locations during the NH summer and SH summer. Table 3.1 shows the number of days of data at respective TAO buoy locations during the northern and southern hemisphere summer that are included in the correlation. I use the *t*-statistic to test the statistical significance of correlation coefficients. Since the mean period of the ISO is 40 days, I conservatively use N/40 as the number of degrees of freedom, where N represents the number of days of data at a particular TAO buoy location. Correlation coefficients maximize at values greater than 0.6 during NH summer, and 0.4 during SH summer, values significantly different from zero at 90% confidence

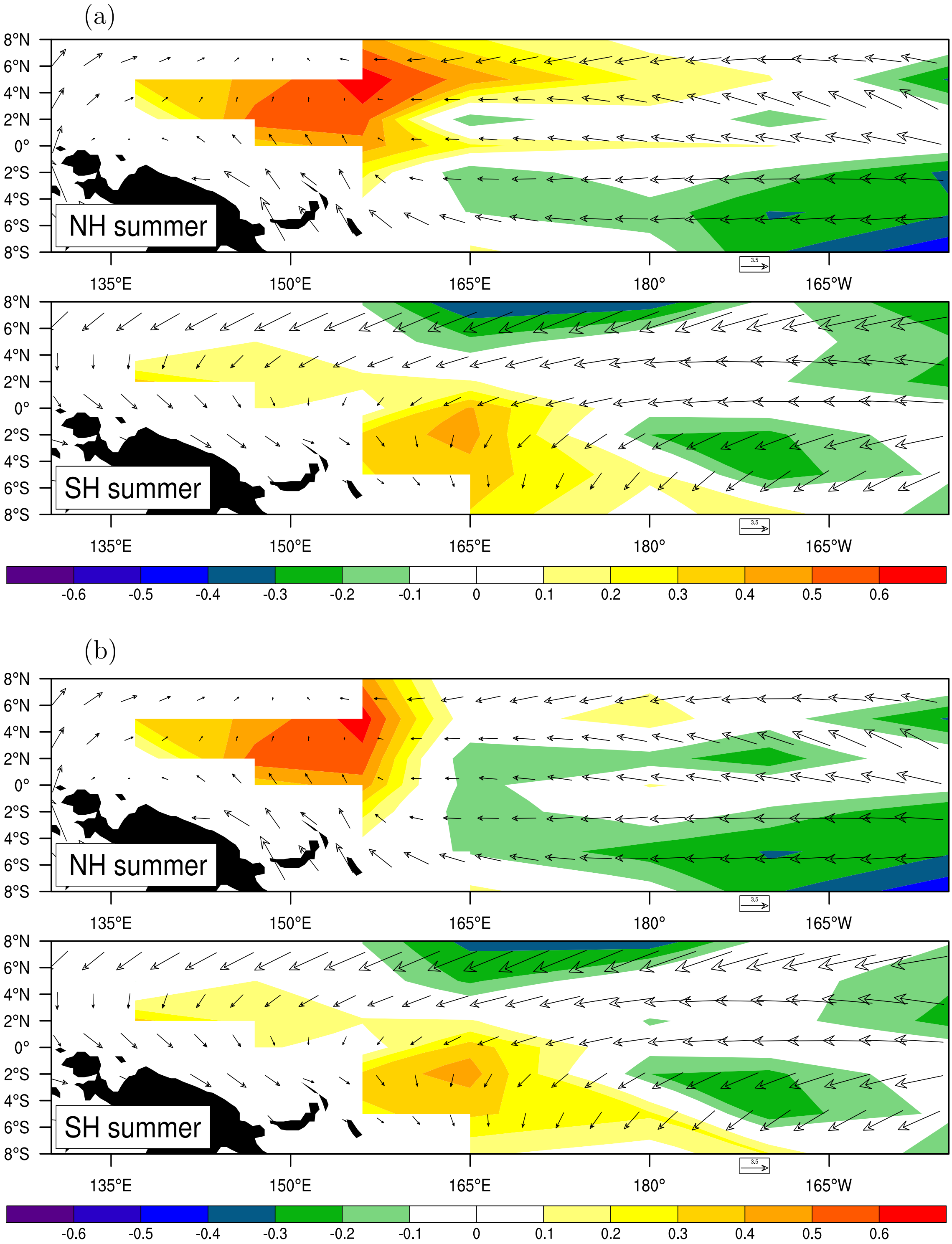

FIGURE 3.4. *Correlation of latent heat flux and Precipitation a) Latent heat flux computed using scalar wind speed b)Latent heat flux computed using vector wind speed. Wind vectors are the mean QuikSCAT wind*

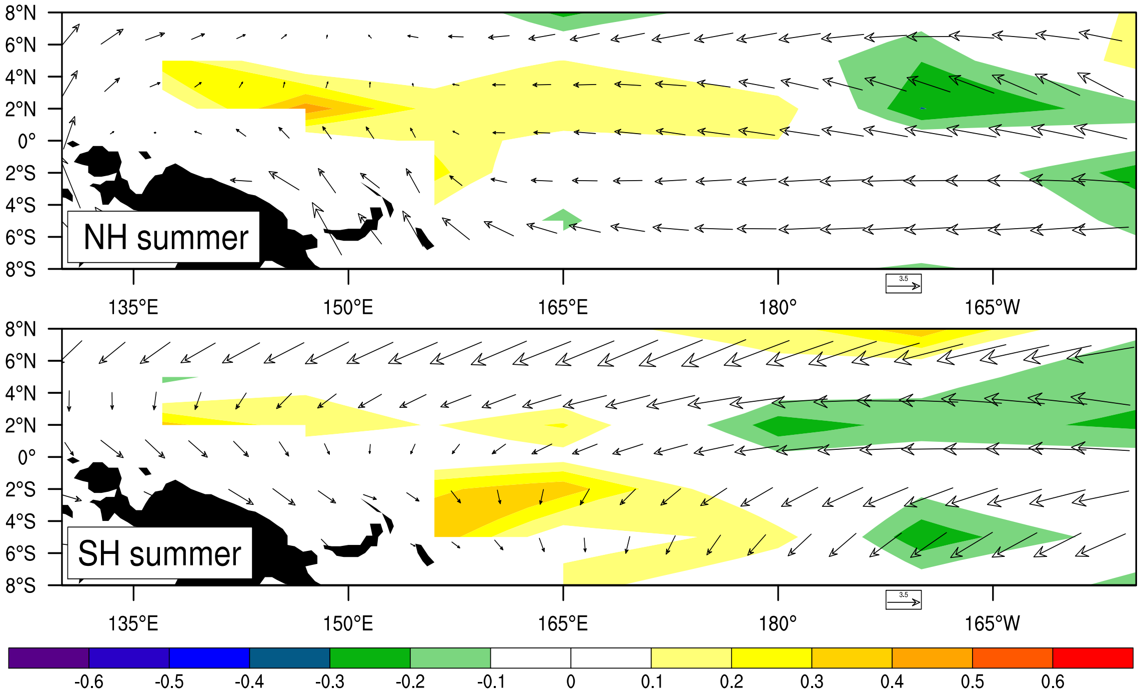

FIGURE 3.5. *Correlation of latent heat flux (computed using 3 day running mean vector winds) and precipitation. Wind vectors are the mean QuikSCAT wind*

level. The maximum correlations occur within the regions of greatest intraseasonal precipitation variance in Figure 3.1, and are also the regions of strongest ISO precipitation anomalies, as will be shown below. Mean wind vectors of Figure 3.1 indicate that the highest correlations occur in regions where the mean flow is weak or slightly westerly. It is observed that the correlation between scalar wind speed and precipitation anomalies (Figure 3.2 a) are qualitatively slightly greater than the correlation of latent heat flux and precipitation anomalies. Correlation of vector wind speed and precipitation (Figure 3.2 b) shows similar correlation as that of latent heat flux and precipitation anomalies during the NH summer, but the correlation during the SH summer seems to be higher. To determine whether these correlations change when using different precipitation product, CMAP (Cli-

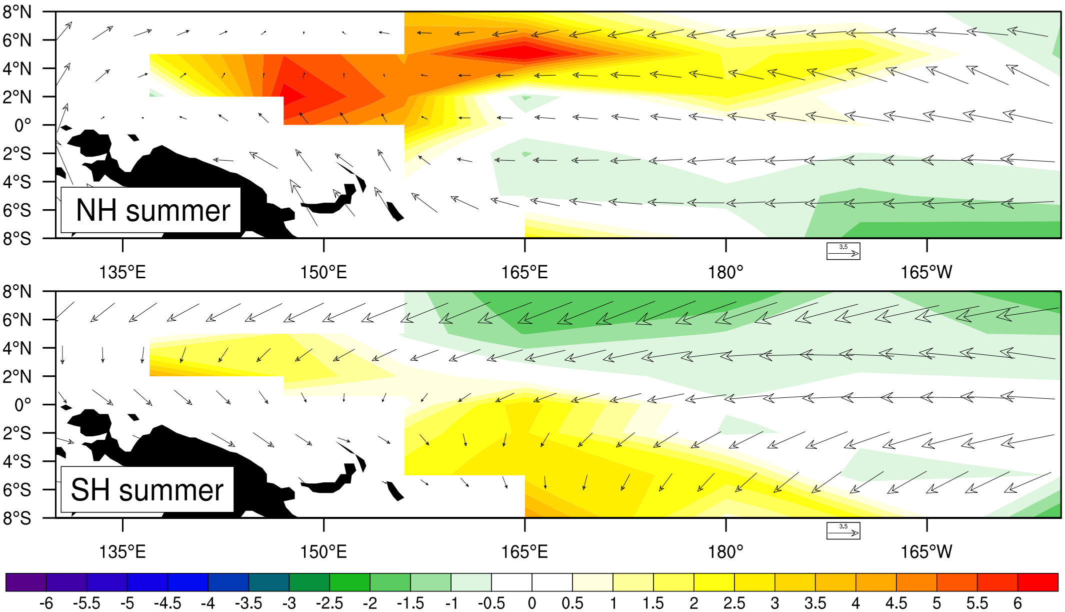

FIGURE 3.6. *Regression of TAO buoy latent heat flux and TRMM precipitation anomalies* (Wm^{-2}/Wm^{-2}) *for Northern (NH) and Southern (SH) hemisphere summer. Wind vectors are the mean QuikSCAT wind*

mate Prediction Center (CPC) Merged Analysis of Precipitation) $2.5^o \times 2.5^o$ grid precipitation data interpolated to the buoy sites were used. The CMAP precipitation data set is a merged product based on gauge observations, satellite estimates (infrared and microwave), and numerical model output. The correlation of buoy latent heat flux and CMAP precipitation was similar to the correlation of buoy latent heat flux and TRMM precipitation, and is thus not shown. Outside the regions of strong intraseasonal precipitation variability, negative correlations exist between latent heat flux and precipitation. These are regions of weak precipitation anomalies and lower sea surface temperatures where large-scale flow anomalies are controlled remotely by diabatic heating processes in the regions of strong intraseasonal precipitation variance.

I do a couple of sensitivity test to examine the impact of short timescale wind variability on the precipitation-latent heat flux correlations. These tests successively minimize the effects of mesoscale gustiness and other short timescale variability of timescale less than 6 days on the latent heat flux. First, daily averaged wind vector components from TAO buoy were used to compute the vector wind speed. Latent heat flux was then re-computed using this vector wind speed (e.g Esbensen and McPhaden 1996). The correlation of latent heat flux, computed using vector winds, and precipitation was similar to that using the scalar wind speed (Figure 3.4(b)). Next, I take a 3 day running mean of u and v component to remove the effect of all short timescale ($< 6day$) wind fluctuations on the latent heat flux-precipitation correlation on the wind speed. Correlation of latent heat flux, computed using the three day running average vector wind speed, and the precipitation decreases to 0.2 for the northern hemisphere summer and 0.3 for the southern hemisphere summer (Figure 3.5), indicating that high frequency wind form an important part of the instantaneous correlation between precipitation and latent heat flux. The enhancement of a mesoscale circulations forced by convection itself may contribute to the increase in positive correlation between intraseasonal latent heat flux and precipitation (Esbensen and McPhaden 1996), although minimizing the influence of other short timescale variability such as easterly waves (3-5 day timescales, e.g. Maloney and Dickson 2003) likely also contributes to the reduction in correlation. A similar result was obtained in section 3.2 when QuickSCAT wind speed is averaged over a larger grid to reduce the impact of high wavenumber spatial features on the wind speed, and correlations were decreased (Figure 3.3).

Lee et al (2001) suggest that divergent circulations associated with deep tropical convection export moist static energy at a rate of about 20% of precip-

Number of days at each buoy location					
Buoy location	NH sum	SH sum	Buoy location	NH sum	SH sum
2^oN137^oE	45	202	5^oS180^oW	899	1002
5^oN137^oE	355	351	2^oS180^oW	1247	1229
8^oN137^oE	49	47	0^oN180^oW	853	849
0^oN147^oE	702	468	2^oN180^oW	752	1051
2^oN147^oE	536	475	5^oN180^oW	1068	1081
5^oN147^oE	902	618	8^oN180^oW	389	399
5^oS156^oE	908	854	8^oS170^oW	1251	1135
2^oS156^oE	755	570	5^oS170^oW	730	713
0^oN156^oE	561	743	2^oS170^oW	820	870
2^oN156^oE	853	635	0^oN170^oW	954	924
5^oN156^oE	800	828	2^oN170^oW	851	874
8^oN156^oE	828	539	5^oN170^oW	458	721
8^oS165^oE	417	709	8^oN170^oW	1104	1220
5^oS165^oE	781	779	8^oS155^oW	811	939
2^oS165^oE	308	303	5^oS155^oW	730	713
0^oN165^oE	122	462	2^oS155^oW	598	667
2^oN165^oE	332	570	0^oN155^oW	926	1023
5^oN165^oE	752	593	2^oN155^oW	987	906
8^oN165^oE	771	769	5^oN155^oW	891	982
8^oS180^oW	884	1050	8^oN155^oW	656	857

TABLE 3.1. *Number of days at each buoy location during Northern hemisphere summer and Southern hemisphere summer.*

itation during strong intraseasonal convective events. Therefore, to support an ISO convective instability, a moist static energy source such as cloud radiative heating or surface latent heat flux must overcompensate for this loss of energy by export. Lin and Mapes (2004) documented the moist static energy source due to cloud-radiative feedbacks, and found it to be about 10-15% of precipitation. Here I quantitatively determine the strength of surface latent heat flux anomalies relative to precipitation anomalies to determine whether wind-induced latent heat fluxes are sufficient to compensate for moist static energy transport out of the atmospheric column during intraseasonal convective events. I note that the implied moist static energy transports due to deep convection are based on theoretical considerations using a first baroclinic mode convective heating profile (e.g. Yu and Neelin 1998). In reality, modest variations in the heating profile vertical structure can cause the amount of energy exported by convective circulations to vary significantly (e.g Kiladis et al. 2005). However, data limitations prevent us from examining full energy budgets, including export. The ability to derive energetically consistent budgets based on reanalysis products on intraseasonal timescales is somewhat doubtful, and so I do not attempt to explicitly calculate moist static energy budgets during intraseasonal precipitation events here.

A linear regression is done between intraseasonal latent heat flux and precipitation to quantify the impact of latent heat flux on the moist static energy budget (Figure 3.6). The regression coefficient of the latent heat flux anomalies and precipitation indicates that for each unit of latent heat flux, about 6 units of precipitation is generated over the enhanced precipitation region during the northern hemisphere summer and about 4 units of precipitation during the southern hemisphere summer. Latent heat contributes about 20% of the total precipitation anomalies, a magnitude approximately sufficient to support a flux driven convective instability. One question is whether the regression coefficients are sensitive to the precipitation dataset used. To test this issue, CMAP (Climate Prediction Center (CPC) Merged Analysis of Precipitation) $2.5^o \times 2.5^o$ grid precipitation data interpolated to the buoy sites were used. The regression of buoy latent heat flux and CMAP precipitation was similar to the regression of buoy latent heat flux and TRMM precipitation, and is thus not shown.

The regressions coefficients of figure 3.6 provide an interesting analysis of the intraseasonal moisture budget. If the intraseasonal moisture balance is dominated by evaporation, precipitation and moisture convergence, the figure 3.6 regressions support the conclusion of Bretherton et al. (2004) that moisture convergence must strongly augment the amount of precipitable water available for precipitation, even with significant forcing by surface fluxes. In the region of high time-mean precipitation the vertically integrated storage term is typically small, and therefore the moisture budget equation represent an approximate balance between moisture convergence, precipitation and evaporation.

$$\langle\frac{\partial q}{\partial t}\rangle \cong 0 \cong -P + \langle\nabla\cdot\vec{V}q\rangle + E \tag{3.1}$$

Since intraseasonal evaporation is 20% of precipitation, a substantial moisture convergence feedback is necessary that augments the amount of water vapor available for intraseasonal precipitation.

3.4. Composite analysis of Wind speed and Precipitation Analysis

Now, the tropical intraseasonal oscillation (ISO) is explicitly examined. Wind and precipitation anomalies are analyzed over the west Pacific during an ISO life cycle. QuikSCAT vector winds, wind speed and TRMM precipitation fields were first bandpass filtered to 30-100 days using a linear non-recursive filter. A composite lifecycle is then constructed using the ISO index of Maloney and Kiehl (2002) as described in section 2.2.1 . Each ISO event is then broken into nine phases as described above. Since ISO events go through a composite cycle in approximately 40 days the average time between phases is approximately 5 days. Composite events were generated by averaging data at each phase across all ISO events.

Since the character of the ISO changes as a function of season, we carry out the analysis separately with respect to the NH summer (May, June, July, August, September, October) and the SH summer (November, December, January, February, March, April). Figure 3.7 shows composite west Pacific ISO vector wind and precipitation anomalies for NH summer, and figure 3.8 shows a similar plot for ISO vector wind and wind speed anomalies. During phase 1, westerly anomalies associated with ISO prevail over most of west Pacific region. Suppressed precipitation occurs to the west of 165^oE centered in the northern hemisphere. Negative wind speed anomalies occur during phase1 (Figure 3.8), since the mean winds are easterly (e.g. Figure 3.1) and anomalous winds associated with ISO are generally westerly across much of the region to the west of 150^oE. During phase 2, the suppressed precipitation region is spatially distributed over somewhat larger area. The easterly wind anomalies associated with ISO becomes weaker. Evidence of eastward and northward movement of suppressed precipitation and westerly winds occurs.

During Phase 3, suppressed precipitation peaks near the northern boundary, and winds are in transition phase from westerly to easterly anomalies. In Phase 4, the suppressed precipitation has moved northward further. Wang and Rui (1990b) observed that both northward and eastward movement of the ISO often occur

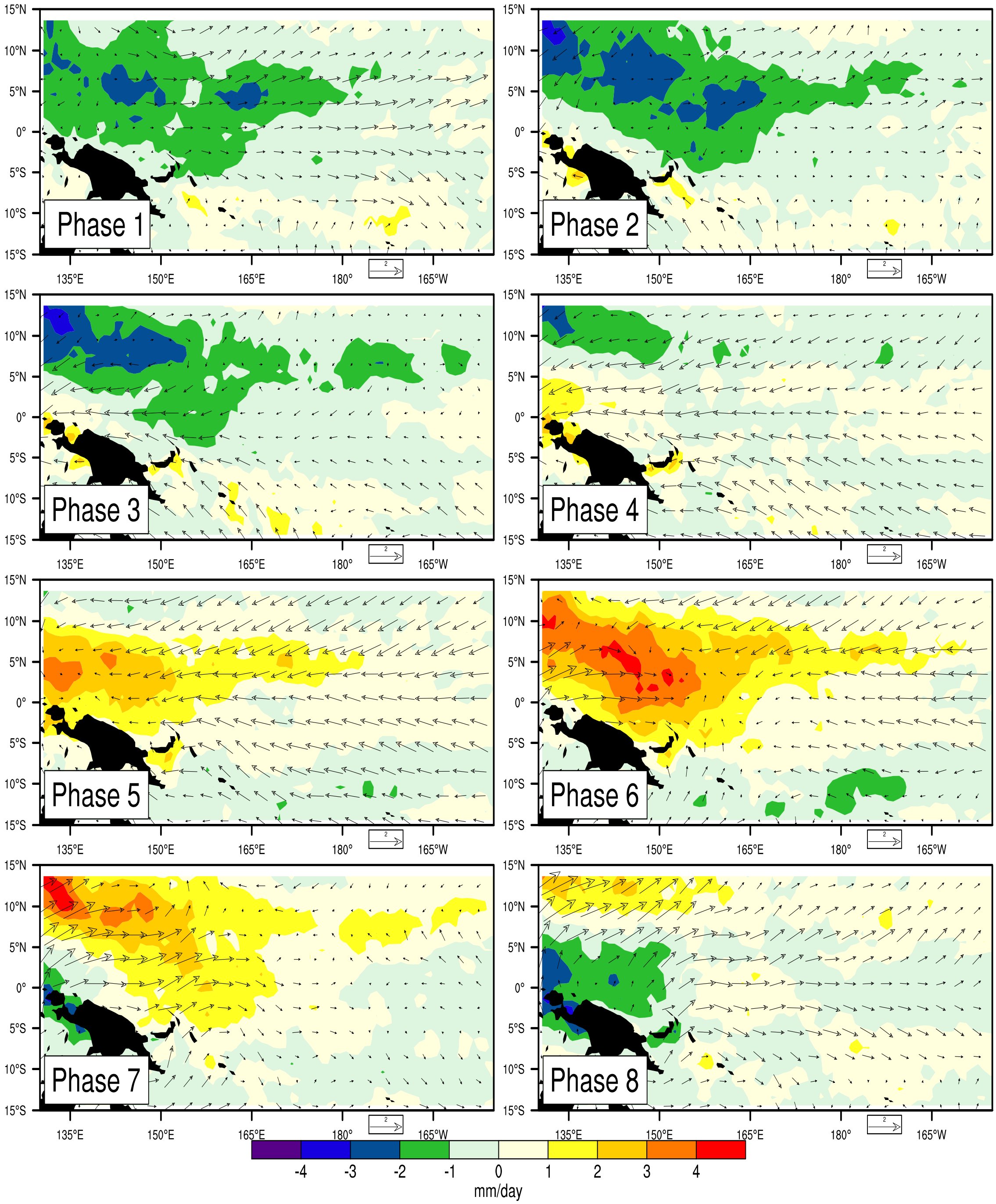

FIGURE 3.7. *Composite of Intraseasonal wind vectors and Precipitation* (*mmday*$^{-1}$) *during the Northern hemisphere summer.*

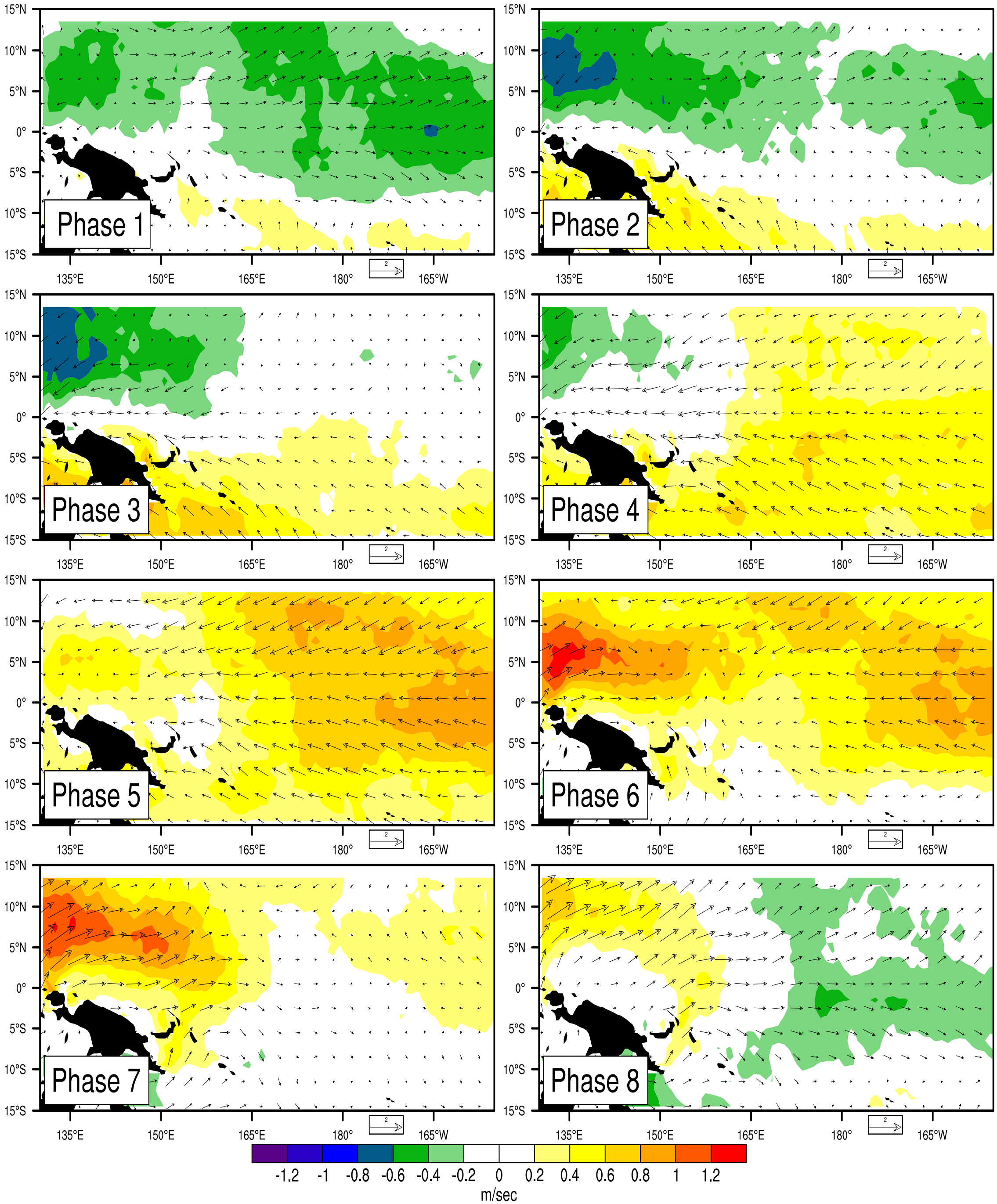

FIGURE 3.8. *Composite of Intraseasonal wind vectors and Wind speed* (ms^{-1}) *during the Northern hemisphere summer.*

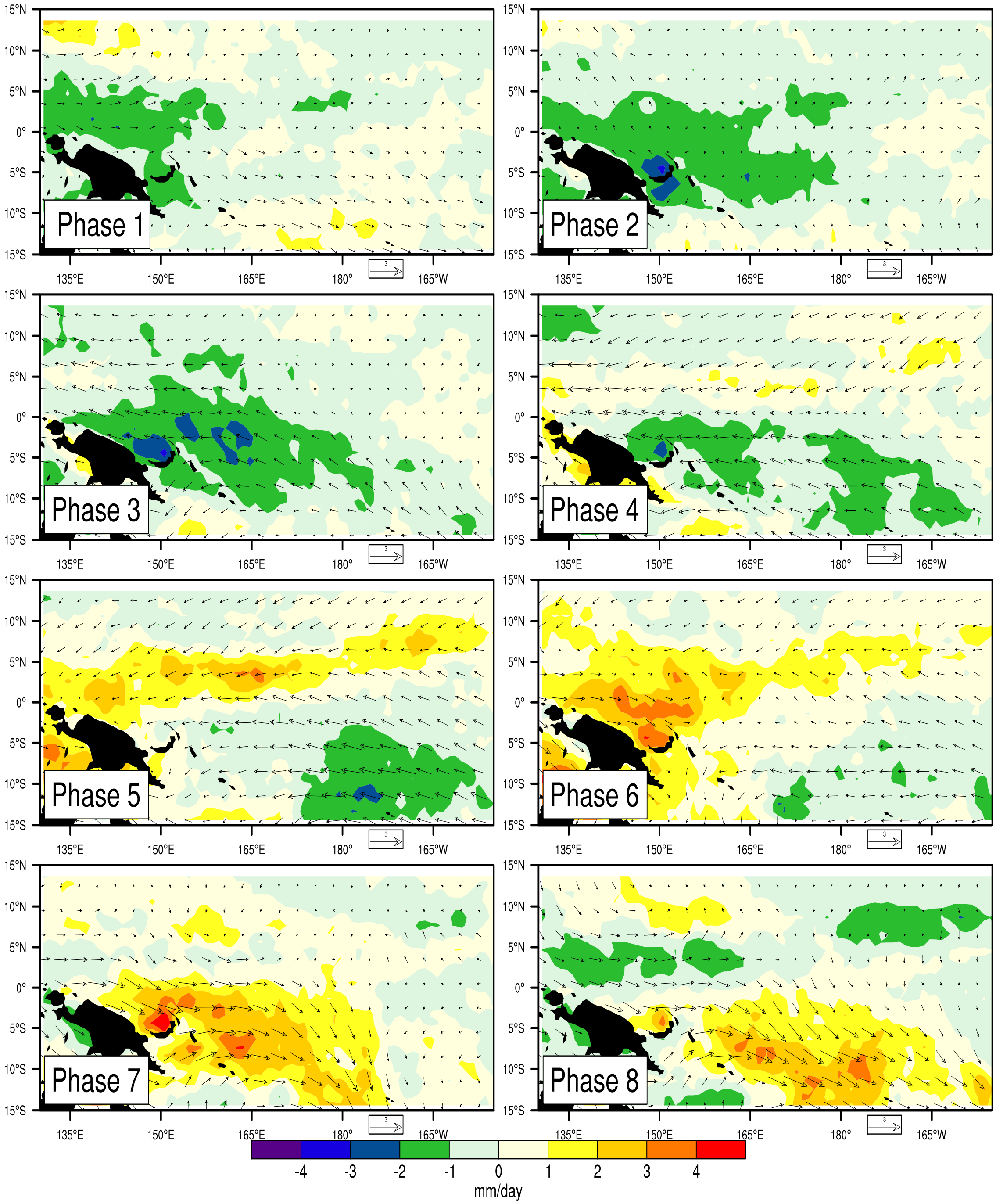

FIGURE 3.9. *Composite of Intraseasonal wind vectors and Precipitation* ($mmday^{-1}$) *during the Southern hemisphere summer.*

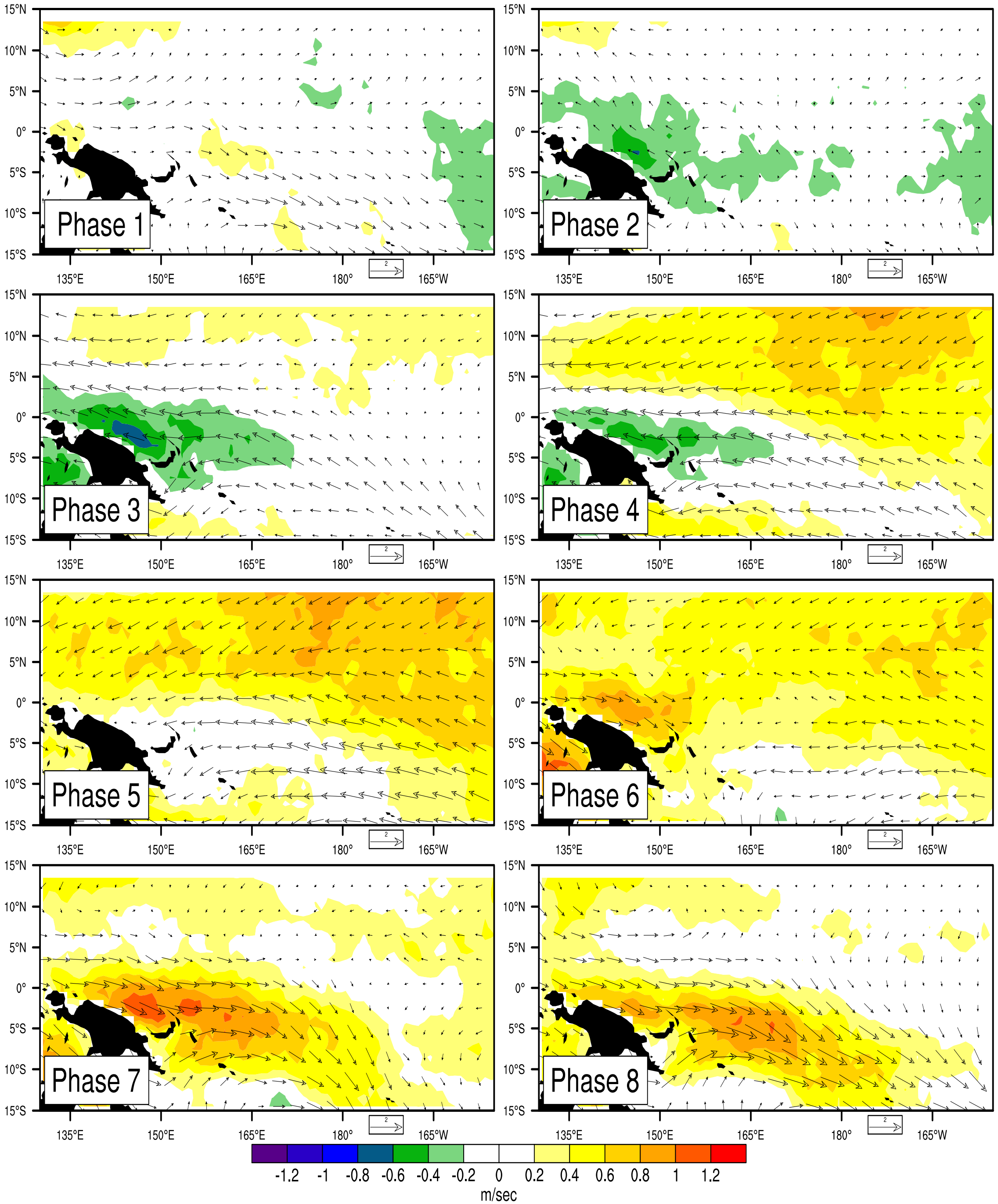

FIGURE 3.10. *Composite of Intraseasonal wind vectors and wind speed* (ms^{-1}) *during the Southern hemisphere summer.*

over the west Pacific during May through October. In phase 4, the anomalous winds are north easterly in the northern hemisphere and south easterly in the southern hemisphere. The meridional convergence onto the equator suggests that frictional convergence occurs during this phase. Maloney and Hartmann (1998) found that such convergence tends to moisten the atmospheric boundary layer, thus preconditioning the lower atmosphere for a subsequent ISO enhanced convective event to occur.

Enhanced convection tends to develop in phase 5 over the region where wind anomalies change from easterly to westerly. To the east of 155^oE the easterly wind anomalies associated with ISO and the mean easterly wind cause positive wind speed anomalies. During phase 6, the enhanced convection moves further eastward and northward . Peak convection is associated with westerly anomalies near and to the west of the convection, and weak easterly anomalies to the east. The westerly anomalies and the region of enhanced convection are nearly in phase as has been observed over the west Pacific region (e.g. Zhang 1996). Wind speed anomalies peak slightly to the west of the enhanced precipitation anomalies. In phase 7 the enhanced precipitation anomalies move northward along with westerly anomalies to the west of 165^oE. In phase 8, westerly anomalies prevail over most of the west Pacific region, and equatorial suppressed precipitation anomalies develop in the wake of the enhanced precipitation anomalies, where the westerly wind anomalies begin to weaken.

Figure 3.9 and figure 3.10 shows similar composites as for Figure 3.7 and 3.8, but for SH summer. During SH summer, phase 1 shows the development of suppressed precipitation anomalies in the vicinity of New Guinea. In phase 2, this region of suppressed precipitation anomalies begins to move southeastward. Wang and Rui (1990b) have observed that November-April ISO anomalies move eastward along the equator until 100^oE when they begin a southeast movement along the mean position of the South Pacific Convergence Zone and Australian monsoon convection. In phase 3, suppressed precipitation anomalies peak in association with easterly anomalies. Anomalous winds associated with ISO are southeasterly in the south Pacific convergence region, with very weak wind anomalies over rest of the region. Wind speed is suppressed near and to the west of the region of suppressed precipitation. In phase 4, the winds are nearly north easterly in the northern hemisphere and south easterly in the southern hemisphere, suggesting meridional convergence onto the equator. In phase 5 convection begins to build near New Guinea, where the easterly anomalies have weakened. The precipitation anomalies move southeastward during phase 6, and wind anomalies become westerly over the region of positive precipitation anomalies. In phase 7 the precipitation anomalies peak with collocated westerly anomalies , similar to the structure of ISO found in west Pacific by Hendon and Salby (1994) and Shinoda et al. (1998). Positive wind speed anomalies peak near and to the west of the region of enhanced precipitation during phase 7. The region of strongest wind speed anomalies generally occurs where westerly anomalies are adding constructively to the mean westerly flow (e.g. Figure 3.1). By phase 8, precipitation, vector wind, and wind speed anomalies propagate eastward along the South Pacific Convergence Zone.

Shinoda et al (1998) suggest that latent heat flux anomalies in the west Pacific warm pool are primarily wind-driven during ISO events (sensible heat flux anomalies are generally small). While thermodynamic-driven perturbations to the surface flux that are associated with ISO-induced SST variations are non-negligible, Shinoda et al. (1998) found that thermodynamic considerations were of second order importance in determining ISO-induced surface flux as compared to the wind-driven component. I will examine this issue more below when examining buoy fluxes to determine the relative contributions of wind speed and thermodynamic anomalies to the anomalous ISO heat flux.

3.5. Eddy contribution in the ISO

A closer scrutiny of the ISO wind speed anomalies is done to determine the portion of the wind speed anomalies that is due to the intraseasonal vector wind anomalies interacting with the mean flow, and the portion to which higher frequency variability such as synoptic transient disturbances provide a contribution. Maloney and Esbensen (2007) found that variations in eddy activity had a substantial impact on intraseasonal wind speed anomalies in the east Pacific warm pool. Further, Maloney and Dickinson (2003) documented a significant modulation of west Pacific eddy kinetic energy by the ISO during boreal summer.

Composite wind speed anomalies were partitioned into Total, Vector and Eddy part, as described in section 2.2.2. During northern hemisphere summer, for both enhanced (phase 6) and suppressed (phase 3) phases high frequency eddy activity contributes about 20% of the variation in the intraseasonal wind speed anomalies on a local basis in the west Pacific (Figure 3.11). During the southern hemisphere summer (Figure 3.12) there is not much contribution from higher frequency eddies in the suppressed phase (phase 3), but about 20% contribution is seen from eddies during the enhanced phase (phase 7) over the tropical west Pacific ocean.

These results suggest that the increase in wind speed during the westerly phase of the intraseasonal oscillation in the west Pacific is due to contribution of the mean wind, the ISO wind vector anomalies and contribution from the higher frequency eddies (less than 20 days). The contribution from eddy activity is observed

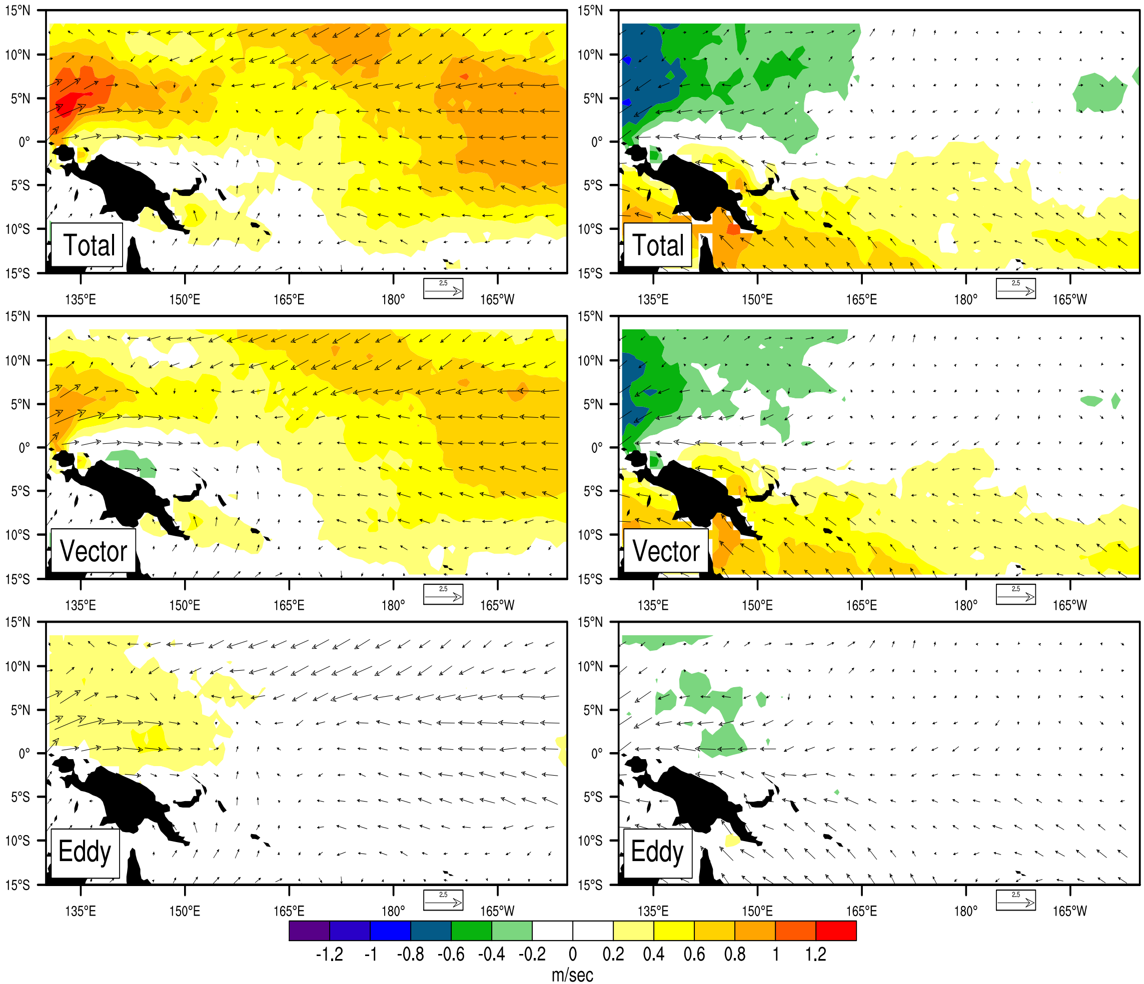

FIGURE 3.11. *Composite of decomposed Intraseasonal wind speed anomalies into Total, Vector and Eddies for the ISO enhanced phase, left panel (Phase 6) and ISO suppressed phase, right panel (Phase 3) during the Northern hemisphere summer. Wind vectors are the intraseasonal QuikSCAT wind.*

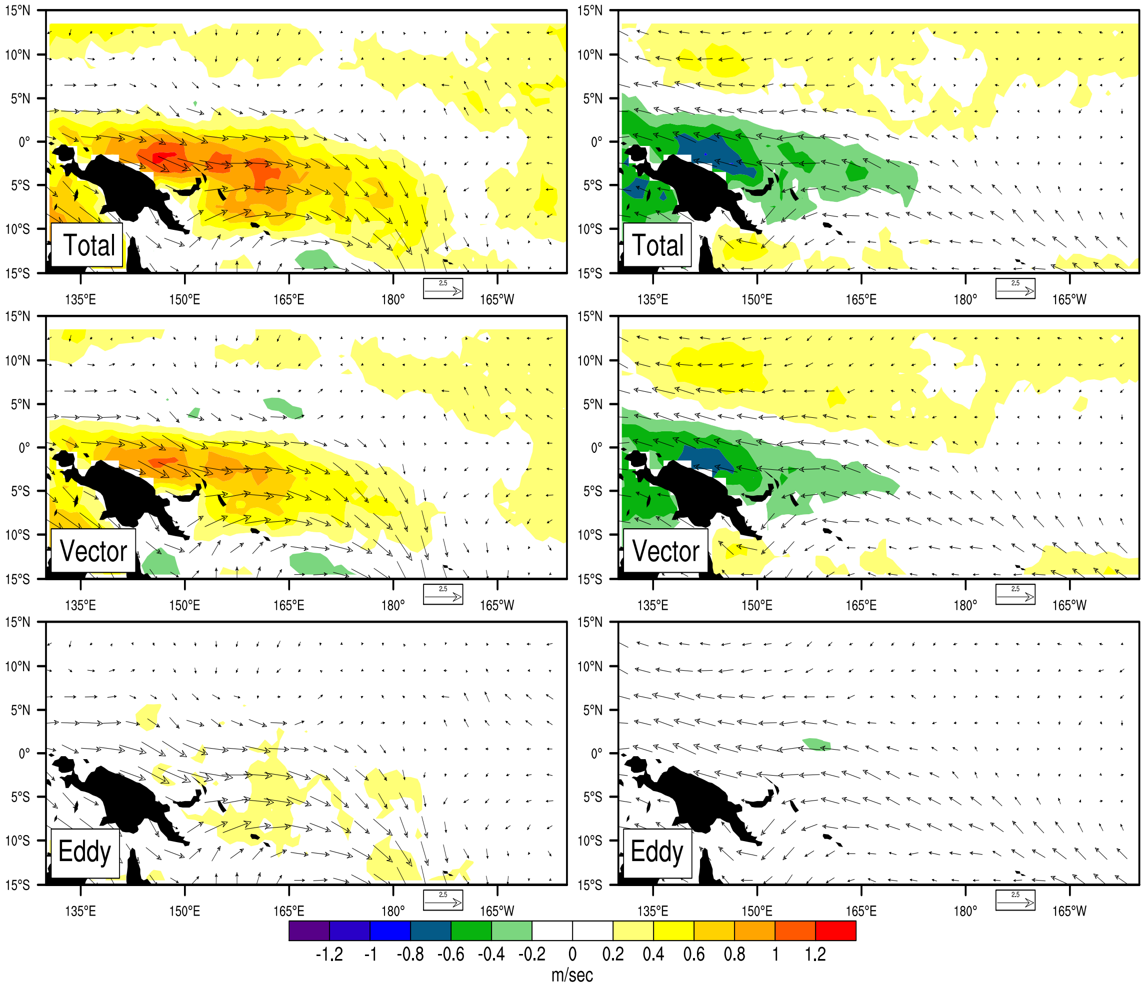

FIGURE 3.12. *Composite of decomposed Intraseasonal wind speed anomalies into Total, Vector and Eddies for the ISO enhanced phase, left panel (Phase 7) and ISO suppressed phase, right panel (Phase 3) during the Southern hemisphere summer. Wind vectors are the intraseasonal QuikSCAT wind.*

during both the enhanced and suppressed phase during the northern hemisphere summer. But during the southern hemisphere summer the contribution of the eddy activity is only during the enhanced phase. Interestingly, this result is opposite to the result found by Maloney and Esbensen (2007) in their study over the east Pacific during the northern hemisphere summer. The eddy variance contributions maximizes over the region where precipitation anomalies peak during the enhanced and the suppressed phases (e.g. Figure 3.7 and Figure 3.9).

The intraseasonal vector-induced component of the wind speed anomaly maximizes to the west of the eddy component and precipitation anomalies in most cases. Thus, the reduction of the wind speed-precipitation correlations observed when high spatial frequency wind components are minimized (e.g see figure 3.2 and 3.3) is consistent with these results. When the part of the wind speed anomaly due to direct interactions between intraseasonal vector wind anomalies and the mean flow are accentuated, the instantaneous correlation between anomalous intraseasonal wind speed and precipitation is reduced.

3.6. Sensitivity test: Are flux anomalies wind-driven?

A sensitivity study is conducted to confirm that the variations in the latent heat flux in the west Pacific are primarily controlled by the wind speed anomalies. The latent heat flux anomaly is partitioned by linearization of the bulk formula for latent heat flux in the following manner.

$$LH' = C(V'\Delta\bar{q} + \Delta q'\bar{V} + (\Delta q'V')') \tag{3.2}$$

where V is the wind speed in the atmospheric boundary layer and Δq is the difference between the saturation specific humidity of the ocean surface and the specific humidity of the atmospheric boundary layer. Overbars represent the sixty days running average, a measure of the basic state derived by averaging fields over the approximate duration of an ISO event. Primes represent intraseasonal anomalies . C is a constant (2756 Jm^{-3}) and represents the product of density, latent heat of vaporization, and the exchange coefficient for evaporation. C was subjectively determined to provide the best fit to the actual latent heat flux anomaly, so it does not account for variations in stability or density that may alter C.

Figure 3.13 shows the linearized latent heat flux anomaly as a function of ISO phase at two buoy locations where we have high regression coefficient during the northern hemisphere summer and the southern hemisphere summer (e.g. Figure 3.6), respectively. The portion of the latent heat flux anomaly due to wind speed alone does a reasonable job of reproducing the actual latent heat flux anomaly. The portion of the latent heat flux anomaly due to thermodynamic anomalies is out of phase with the actual latent heat flux anomaly, and has lesser magnitude. This sensitivity study suggest that ISO-related latent heat flux anomalies are mostly wind-driven, consistent with intraseasonal precipitation anomalies being supported by wind induced surface heat exchange. Figure 3.13 also shows that latent heat flux anomalies are about 20% of precipitation anomalies at the time of maximum precipitation. This result is consistent with that derived in the lag regression plots in Figure 3.6. Precipitation peaks approximately 5 days before the latent heat flux, consistent with the previous studies of ISO using other data products (e.g. Hendon and Glick 1997)

A sensitivity test can also be conducted to determine whether wind speed variability is responsible for the more general correlation between intraseasonal wind speed and precipitation in the west Pacific. Figure 3.14 shows the correlation of TRMM precipitation and buoy latent heat flux anomalies calculated using fixed relative humidity, air temperature and sea surface temperature. The spatial

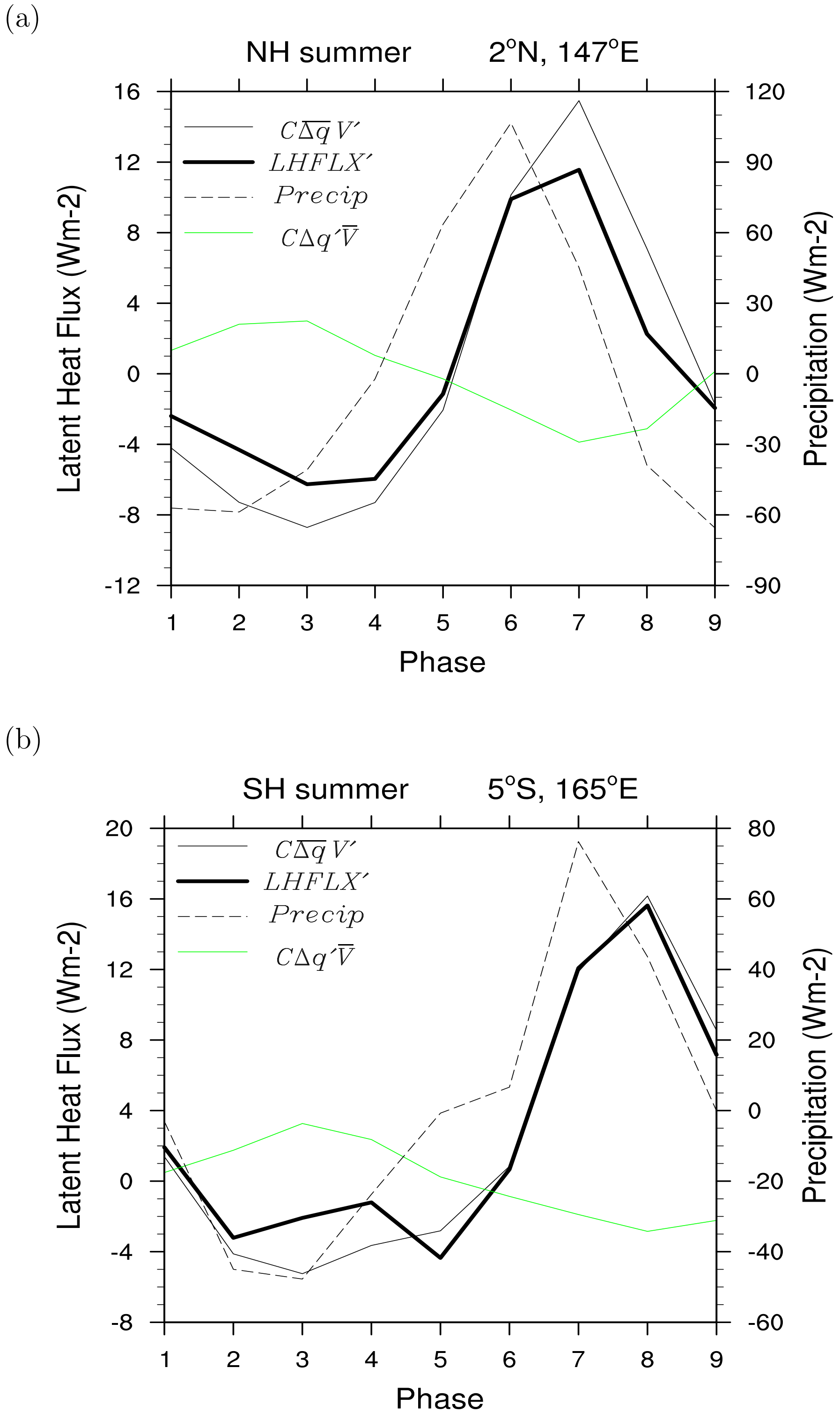

FIGURE 3.13. *Latent heat flux with phase at TAO buoy location a) 2^oN147^oE b) 5^oS165^oE.*

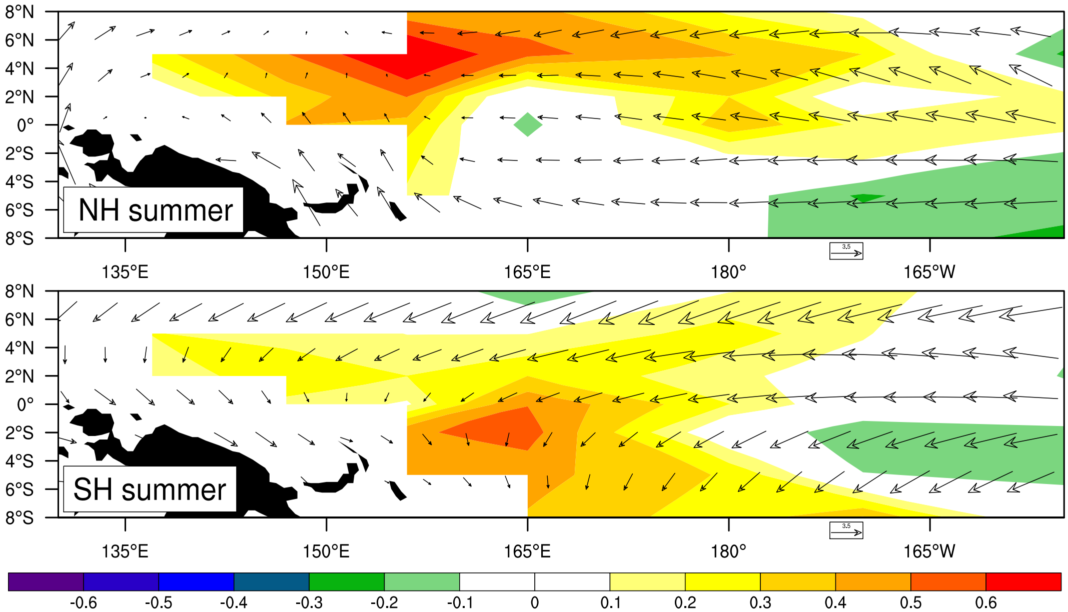

FIGURE 3.14. *Correlation of latent heat flux (fixed specific humidity) and precipitation anomalies*

distribution of the correlation maps is now more similar to the correlation maps of wind speed and precipitation shown in Figure 3.2 b. Anomalies in air-sea humidity difference seem to be contributing towards the negative correlation of latent heat flux and precipitation in Figure 3.4 away from the regions where intraseasonal precipitation variance maximizes (e.g. Figure 3.1).

4. INDIAN OCEAN ANALYSIS

Because a buoy array with long data record does not exist over the Indian ocean, an assessment of whether wind induced surface heat exchange is viable mechanism for supporting Indian ocean intraseasonal convection will be conducted only using satellite derived precipitation and winds. Such an analysis will be described in this section.

4.1. 30-100 day Precipitation variance

Figure 4.1 shows that precipitation variance peaks over the east Indian ocean between $5^oN - 5^oS$ during the NH summer, accompanied by other maxima to the west of southern Indian peninsula, in the Bay of Bengal, and in the south China sea. Precipitation variance generally maximizes in the region of high mean precipitation. The mean flow during NH summer shows the well documented Indian ocean monsoonal flow pattern. The mean winds are southeasterly to the south of the equator, transitioning to flow that is southwesterly to the north of 5^oS, with winds becoming westerly just southwest of the Indian peninsula. During this season, the southwest monsoon is the dominant pattern in the North Indian ocean. A monsoon trough and the ITCZ is located over the Indian subcontinent, and the sharp turning of the mean winds near the equator maintains near-geostrophic balance in the presence of this monsoon trough.

During the southern hemisphere summer, precipitation variance peaks between $5^oN - 5^oS$ and has a greater longitudinal extent than during the NH summer. Precipitation variance peaks over the region of high mean precipitation. The ITCZ and monsoon trough are over the South Indian ocean during this period. The convergence of meridional winds is very well pronounced along 10^oS. The

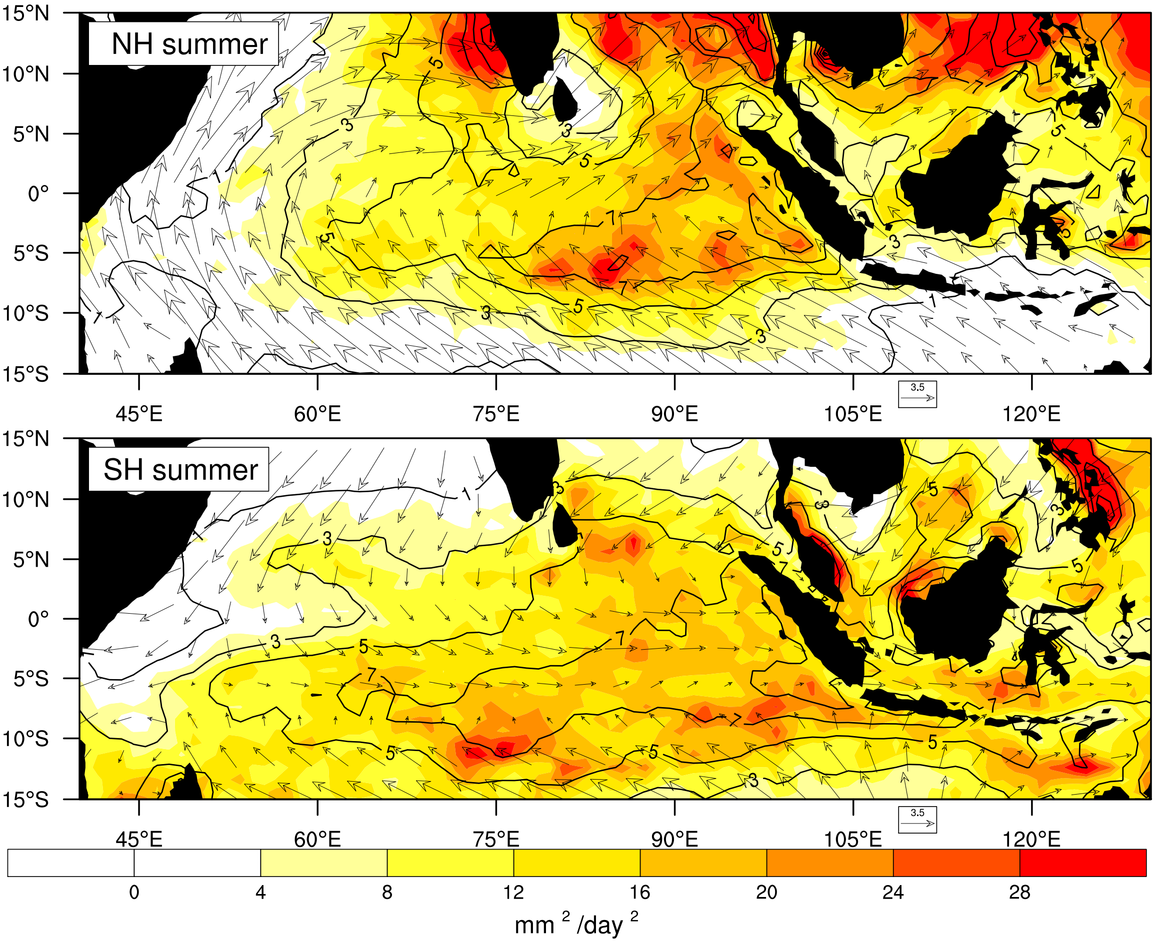

FIGURE 4.1. *Precipitation variance (mm^2day^{-2} filled contour) and mean precipitation ($mmday^{-1}$ line contour) for Northern hemisphere (NH) summer and Southern hemisphere (SH) summer. Wind vectors are the mean QuickSCAT wind.*

North Indian ocean is dominated by northeasterly monsoon flow that crosses the equator and converges into the ITCZ. The mean winds are southeasterly to the south of 10^oS and they meet the cross equatorial flow creating a convergence zone near 10^oS. The mean winds are westerly in the equatorial east and central Indian ocean, near the region where precipitation variance maximizes.

4.2. Correlation of wind speed and precipitation

Figure 4.2 (a) shows the correlation of intraseasonal wind speed and precipitation anomalies over the Indian ocean. Significant positive correlations of 0.7 occur over the regions of large intraseasonal precipitation variance during both the northern hemisphere and the southern hemisphere summer, primarily near regions where the mean flow is westerly. When the vector wind speed is used in the calculation, the correlation decreases to 0.6 during the northern hemisphere and southern hemisphere summer (Figure 4.2 (b)). These correlations over the region of enhanced precipitation variance are significantly different from zero at 90% confidence interval. The correlation of vector wind speed and precipitation further decreases when the vector winds are averaged over a $2.5^o \times 2.5^o$ grid size (Figure 4.3). On the $2.5^o \times 2.5^o$ grid, the correlation during the northern hemisphere summer is 0.2 and that over the southern hemisphere summer is 0.3. These results suggest that higher spatial frequency flow components contribute towards the enhancement of the wind speed, and thus the increases in the positive correlation between intraseasonal wind speed and precipitation. The sensitivity study conducted over the west Pacific suggested that the intraseasonal latent heat flux there is primarily wind driven. If this relationship holds true over the Indian ocean, then the positive correlation of wind speed and precipitation would generate a positive correlation between latent heat flux and precipitation in the region of strong intraseasonal precipitation anomalies. This would suggest that wind induced surface heat exchange plays a role in the enhancement of the precipitation anomalies over the Indian ocean .

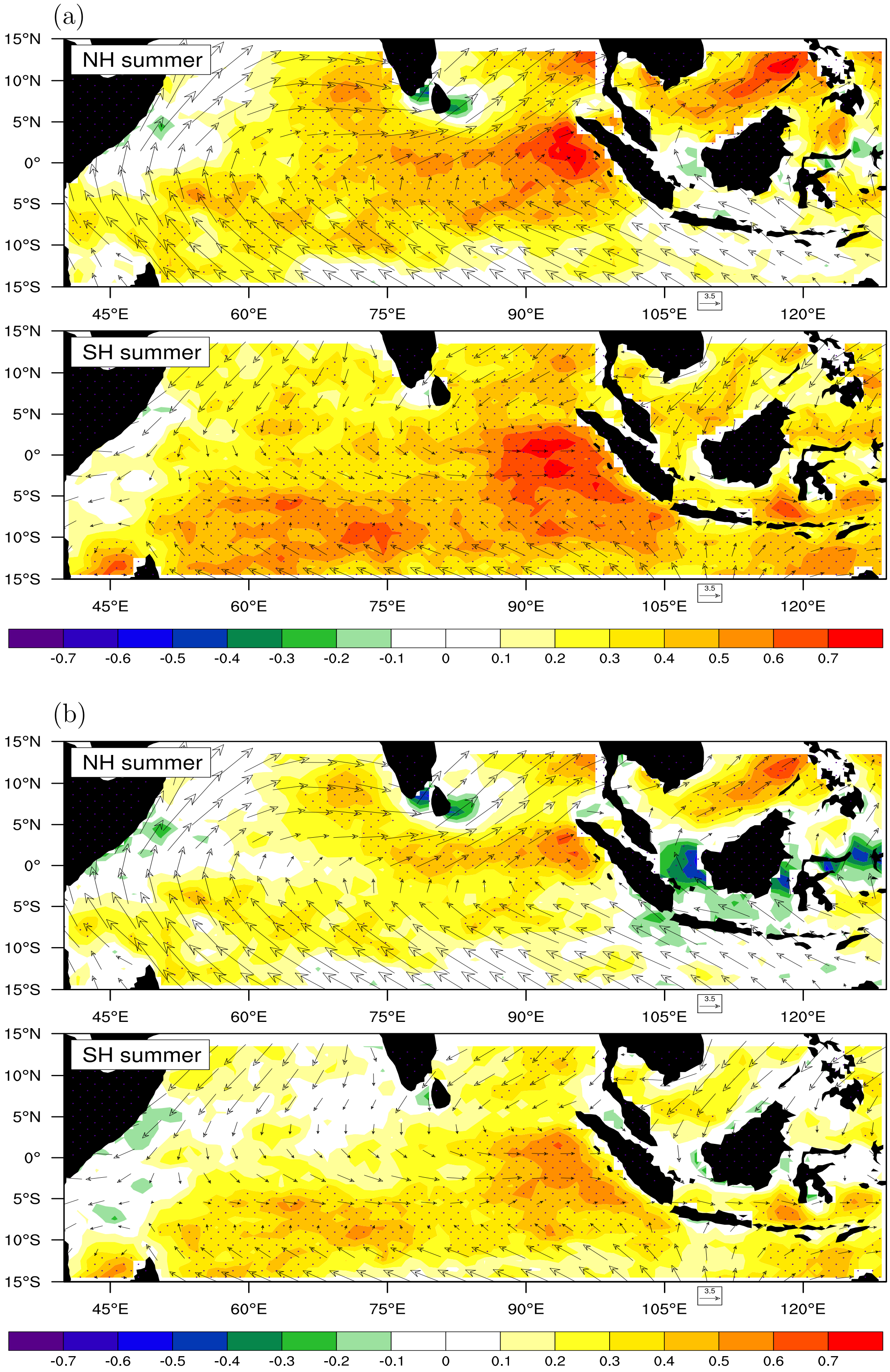

FIGURE 4.2. *Correlation of wind speed and precipitation a) Scalar wind speed b)Vector wind speed. Stippling shows region where the correlation which are different from zero at 90% confidence interval. Wind vectors are the mean QuikSCAT wind.*

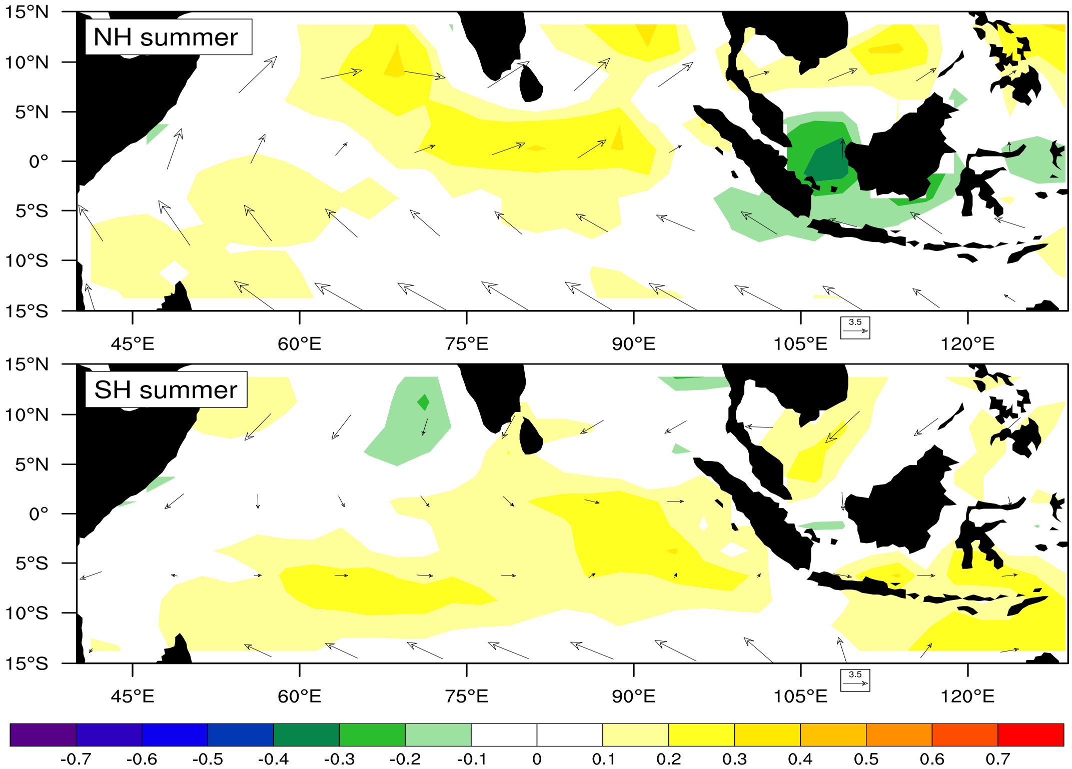

FIGURE 4.3. *Correlation of vector wind speed (computed using 2.5 grid averaged vector winds) and precipitation. Wind vectors are the mean QuikSCAT wind.*

4.3. Composite analysis in the Indian ocean

Figure 4.4 shows a composite lifecycle of ISO vector wind and precipitation anomalies for northern hemisphere summer in the tropical Indian ocean. Figure 4.5 shows a similar composite of ISO vector and wind speed anomalies. During phase 1, a positive precipitation anomaly develops near 70^oE and the equator. Suppressed precipitation anomalies are located in the northern Indian ocean near 10^oN. Weak easterly anomalies exist near the positive precipitation anomalies. At phase 2, positive precipitation anomalies increase in amplitude and spatial extent (from 70^oE to 100^oE). The positive precipitation anomalies appear to develop in place over the Indian ocean rather than propagating eastward, in agreement with

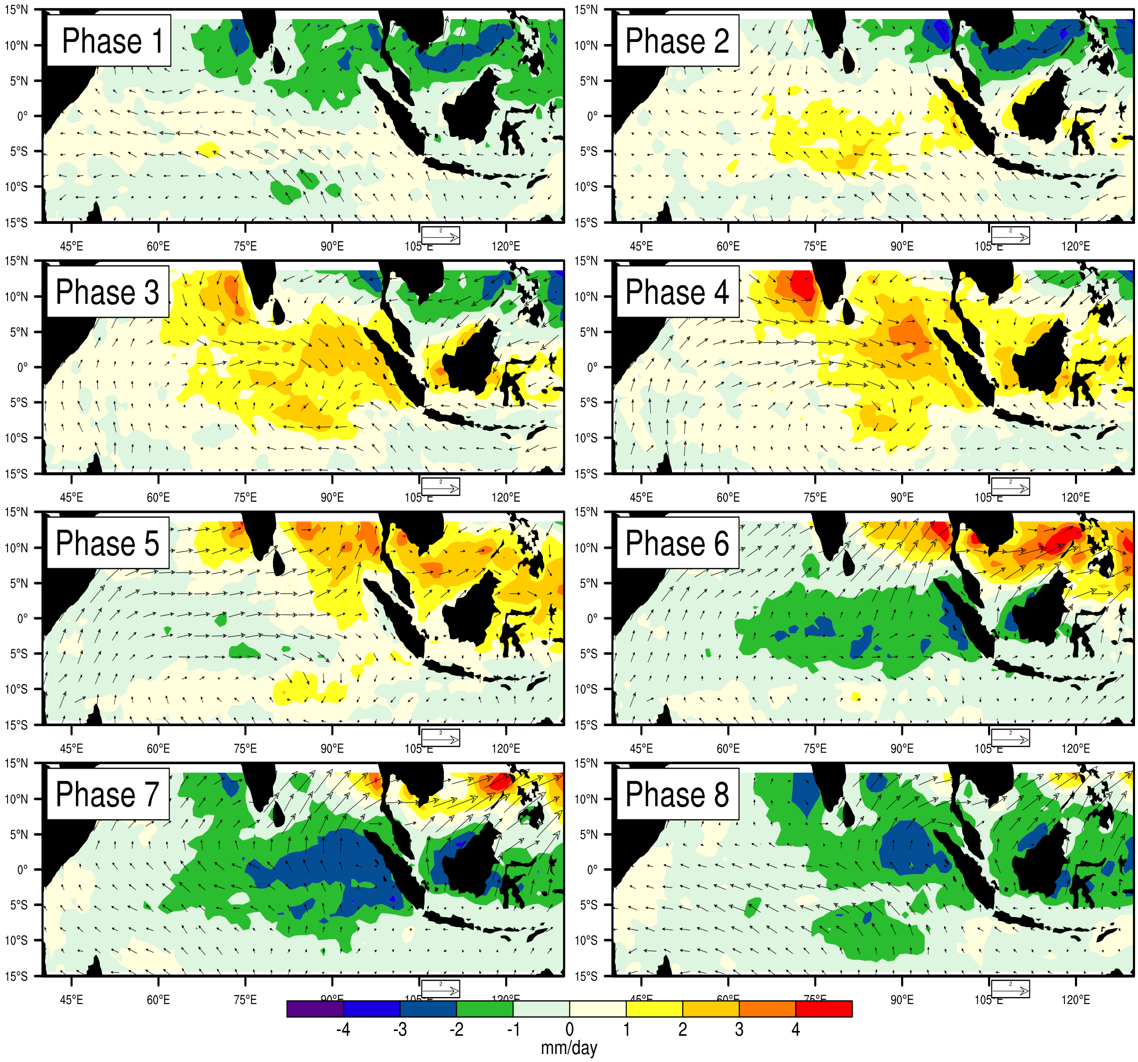

FIGURE 4.4. *Composite of Intraseasonal wind vectors and precipitation (mmday^{-1}) during the Northern hemisphere summer.*

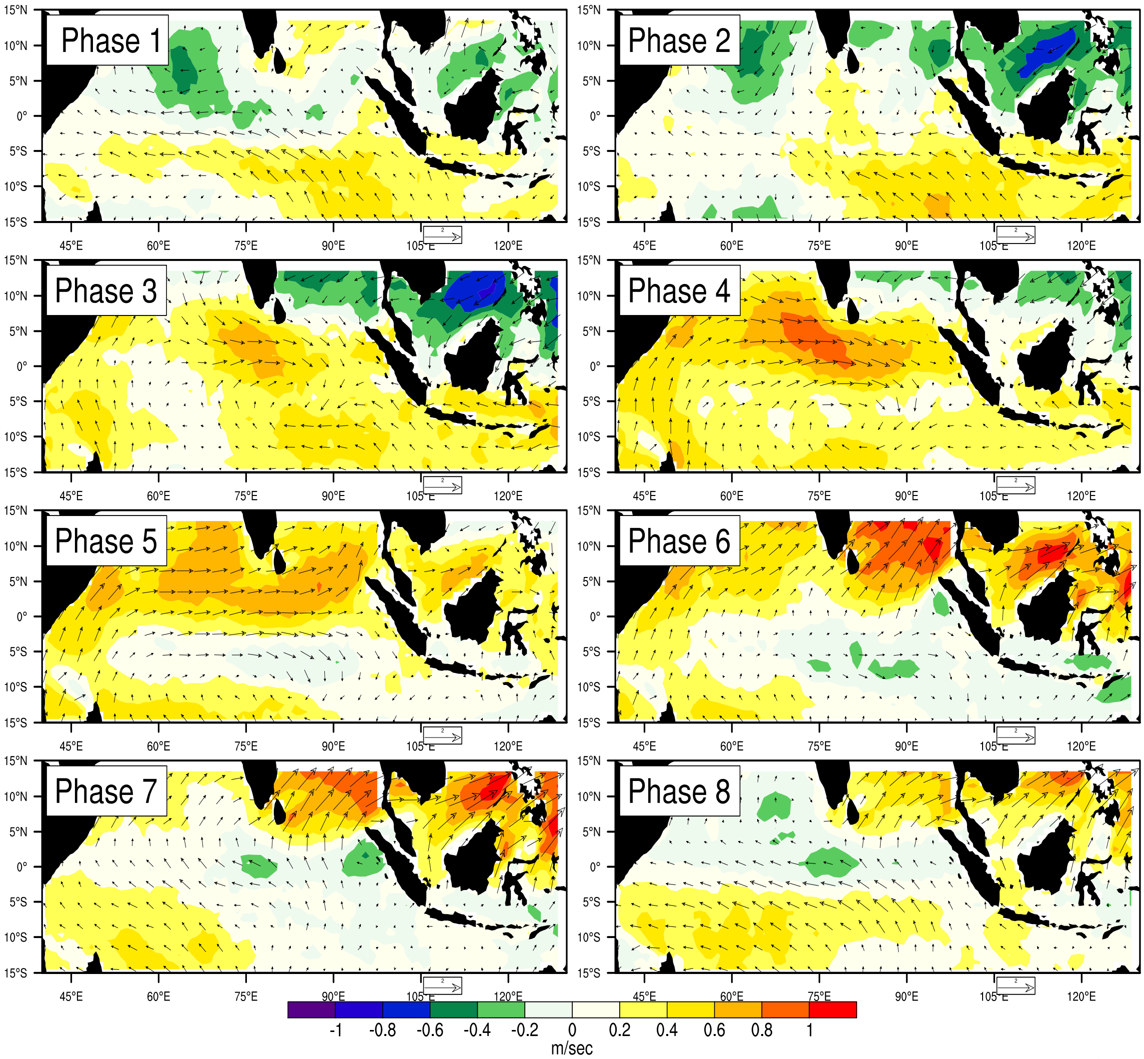

FIGURE 4.5. *Composite of Intraseasonal wind vectors and wind speed* (ms^{-1}) *during the Northern hemisphere summer.*

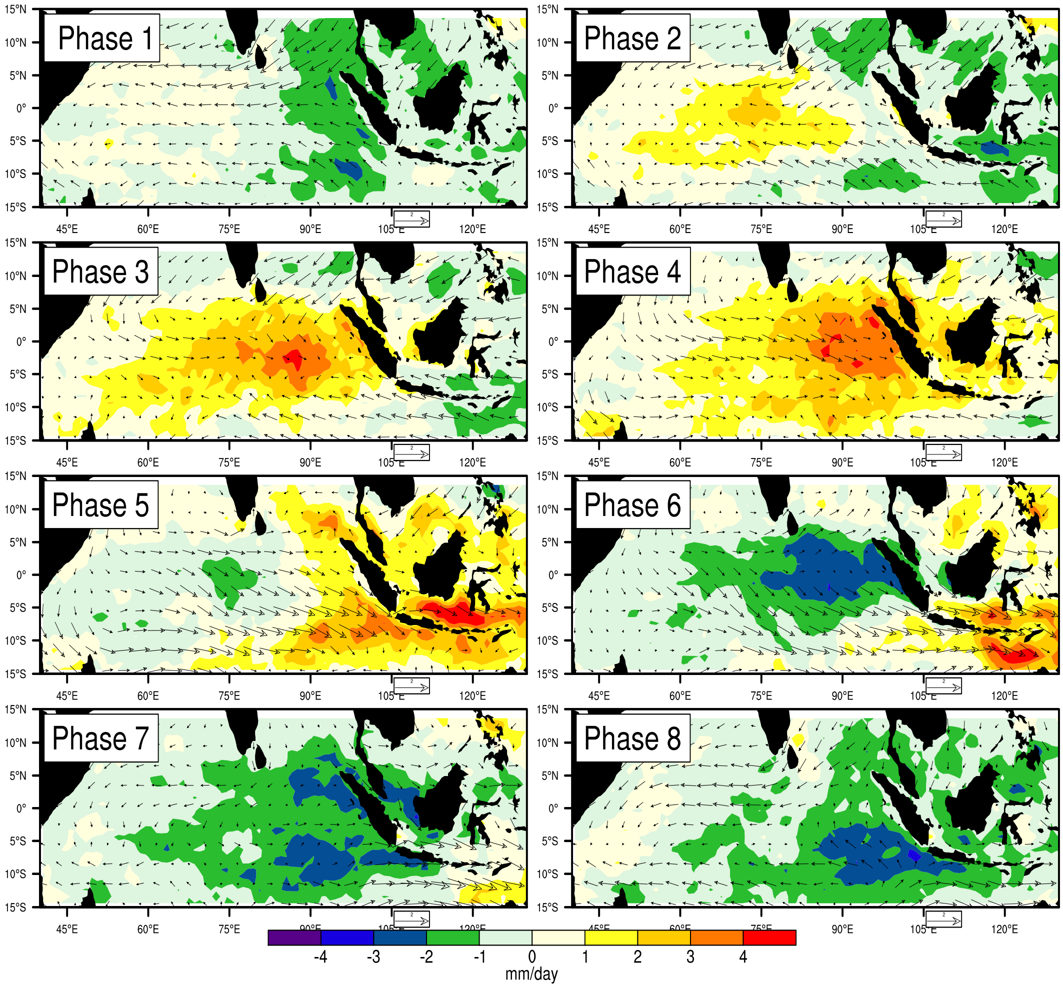

FIGURE 4.6. *Composite of Intraseasonal wind vectors and precipitation ($mmday^{-1}$) during the Southern hemisphere summer.*

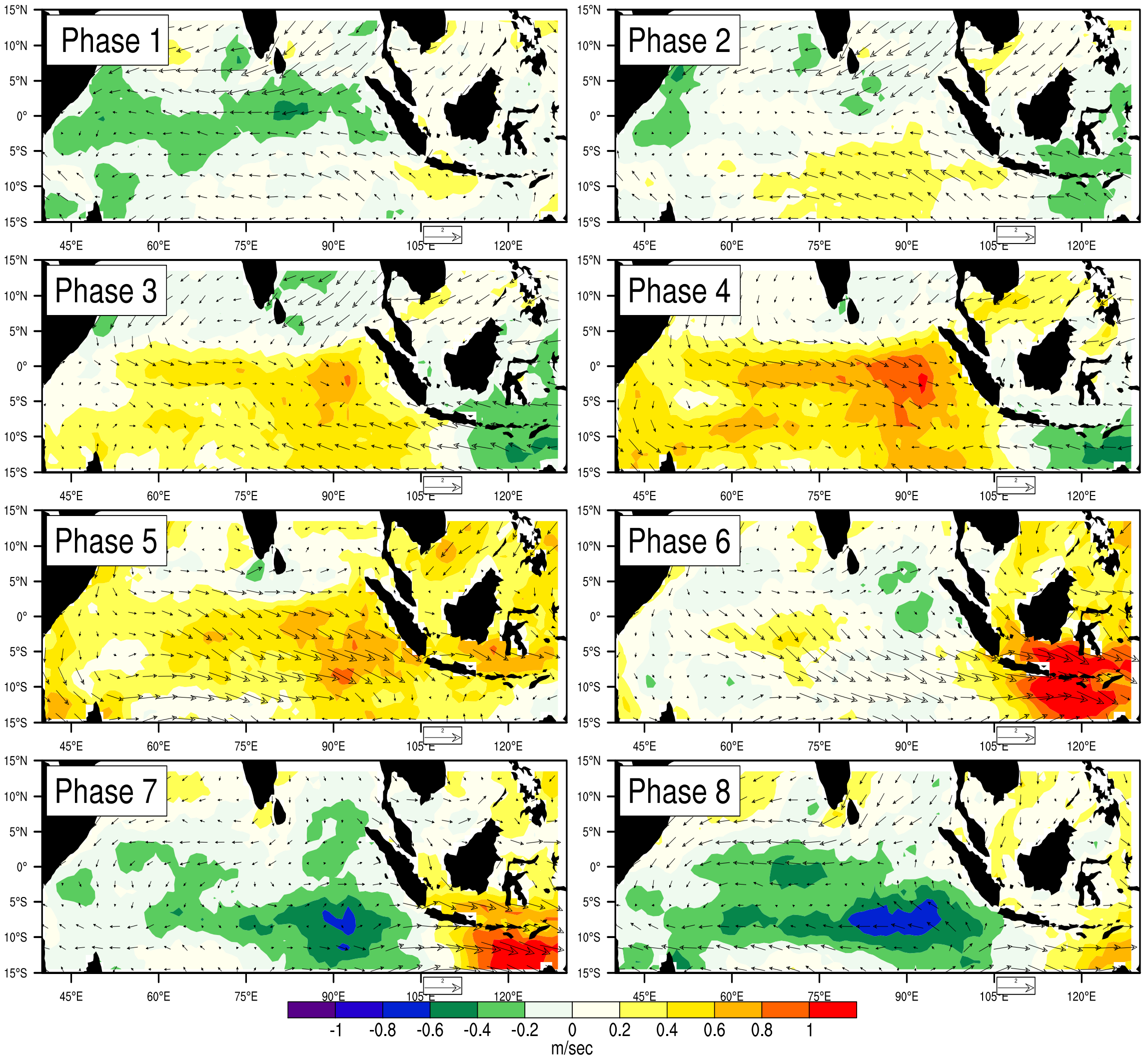

FIGURE 4.7. *Composite of Intraseasonal wind vectors and wind speed* (ms^{-1}) *during the Southern hemisphere summer.*

the observations of Lawrence and Webster (2002), while the suppressed anomalies move northeastward. In phase 3, positive precipitation anomalies begin northward propagation and increase in amplitude. The magnitude of precipitation anomalies to the southwest of the Indian peninsula becomes greater than the precipitation anomalies near the equator . Westerly anomalies develop in association with positive anomalies in precipitation and follow the precipitation anomalies northward. Cyclonic gyres are located to the north and south of equator, consistent with Rossby waves forced by convective heating. Enhanced wind speed develops across much of the Indian ocean during phase 3, peaking near the equator in association with westerly anomalies Figure 4.5. At phase 4, precipitation anomalies peak slightly north of equator at around $90^o E$, and just to the southwest of Indian peninsula. Equatorial westerly anomalies also maximize. Positive wind speed anomalies maximize near and to the southwest of enhanced precipitation anomalies, in association with anomalous westerly flow thus suggesting a lag between the wind speed anomaly and precipitation anomaly. If latent heat flux is primarily driven by wind speed variations, then latent heat flux would peak to the south west of the region of enhanced convection, thus suggesting a lag between the latent heat flux and precipitation anomalies. Hendon and Glick (1997) surmised that the latent heat flux lags the enhanced convection by about 1-2 weeks over the equatorial Indian Ocean. Such a relationship is in agreement with the structure of ISO model I as suggested by Zhang and McPhaden (2000). In Phase 5, precipitation anomalies have moved further northwestward. The cyclonic gyre, in the NH has moved out of the frame but the southern cyclonic gyre has moved more westward. The eastward and northward movement of the precipitation anomalies makes the NH summertime precipitation anomalies appear as a band tilting northwest-southeast with latitude. These results are consistent with those of Lawrence and Webster

(2002) who used OLR data to define atmospheric convection . In phase 6, positive precipitation anomalies have moved northwestward and suppressed anomalies develop from 60 - 105^oE along the equator, where equatorial westerly anomalies weaken dramatically and also propagate northward. Wind speed anomalies are weak during phase 6 along the equator, although strong along 10^oN just to the south of enhanced precipitation. It is noted that the tendency for wind speed and precipitation to propagate northward in tandem is consistent with theoretical work that suggests wind-evaporation feedback is necessary to maintain instability of the monsoonal flow that supports northward propagating intraseasonal wind and precipitation anomalies (Bellon and Sobel 2007). During phase 7, the suppressed precipitation anomalies strengthen, and begin to move eastward and northward, with peak anomalies centered around 90^oE along the equator. Equatorial wind anomalies become easterly, and wind speed is suppressed. Wind anomalies are weak easterly in the southern hemisphere, and north westerly in the northern hemisphere.

Figure 4.6 shows the composite of ISO vector wind and precipitation anomalies for SH summer, and figure 4.7 shows the corresponding composite for vector wind and wind speed anomalies. During phase 1, a positive precipitation anomaly is initiated around 50^oE just south of the equator. Wind anomalies have an easterly component across much of the Indian ocean with meridional convergence onto the equator. Suppressed precipitation anomalies occur during phase 1 around 100^oE. Wind speed is anomalously low along the equator in the region where mean westerly wind anomalies occur (e.g Figure 3.15). During phase 2, the positive anomalies strengthen and expand from $45^oE - 90^oE$, with the highest magnitude at 75^oE. Wind anomalies are weak easterly in the region of positive precipitation anomalies, with north easterly and south easterly wind anomalies to the north and south. There is north-eastward and south-eastward movement of the suppressed precipitation anomalies along with the eastward movement. Wind speed anomalies peak to the south of the positive precipitation anomaly, with negative wind speed anomalies to the east of $110^o E$ and to the east of Africa.

During phase 3, positive precipitation anomalies are near maximum magnitude and move eastward to be centered just south of the equator at $90^o E$. Wind anomalies are westerly near and to the west of the enhanced precipitation anomaly, with northeasterly and southeasterly anomalies to the north and south. Suppressed precipitation anomalies propagate eastward, but also have northeastward and southeastward components. Positive wind speed anomalies are present along the equator in the southern hemisphere, with the highest magnitude wind speed anomalies collocated with the strongest positive precipitation anomalies.

In phase 4, the precipitation anomaly has moved further eastward and are centered to the east of $90^o E$. The magnitude of the peak precipitation anomaly is higher than for northern hemisphere summer . Wind anomalies are westerly to the west of and within the region of enhanced precipitation anomalies. Wind speed anomalies maximize near and to the west of the region where enhanced precipitation anomalies occur. It is interesting that the lag between precipitation and wind anomalies in the Indian ocean during SH summer is less than that found in previous studies (Hendon and Salby 1994, Shinoda et al. 1998) and is more like the observed Pacific relationship (Jones and Weare (1996)). It is possible that better resolution of high spatial wavenumber wind features in QuikSCAT may help explain this result. Figure 4.3 showed that when vector wind components averaged over a $2.5^o \times 2.5^o$ grid were used to compute wind speed, the wind speed-precipitation correlation was reduced. Tropical convection is effective at forcing wind fluctuations of high spatial wavenumber. The Indian ocean precipitation anomaly splits in phase 5, with one part moving northeastward and the other southeastward to be centered near $10^o S$ and extending eastward of $90^o E$. This behavior is consistent with Wang and Rui (1990b) who showed that the ISO convective anomaly moves eastward along equator until $100^o E$, when it splits with one part moving northeastward and the other moving southeastward. They found that the southeast mode occurs exclusively during November-April, indicating a relationship to the Australian monsoon and South Pacific Convergence Zone (SPCZ). The wind speed anomaly maximizes in association with the southeastward moving precipitation anomaly, generally where mean winds are from the west. The northeastward component of the precipitation anomaly is weaker in magnitude than the southeastward moving component. At phase 5, suppressed precipitation is developing near $75^o E$.

During phase 6, the suppressed precipitation anomaly increases in magnitude and moves eastward along the equator. Wind anomalies are southwesterly and northwesterly to the north and south of the suppressed precipitation anomaly, opposite to that of the phase 3. Indian ocean wind speed anomalies are generally weak, although a negative wind speed anomaly is observed over the region of suppressed precipitation. Strong positive wind speed anomalies occur to the south of the maritime continent, beginning to propagate into west Pacific(see figure 3.10). During phase 7, the suppressed precipitation anomaly splits with components to the north and south of the equator. Vector wind anomalies are generally weak over the region of suppressed precipitation, although negative wind speed anomalies are collocated with the southern component of the suppressed precipitation anomaly. During phase 8, the northern component of the suppressed precipitation anomaly weakens and moves northeastward. The southern component of the suppressed anomaly moves generally eastward to be centered to the east of $90^o E$. The southern hemisphere component of the suppressed precipitation anomaly is associated with south easterly wind anomalies. Negative wind speed anomalies occur over the south Indian Ocean, and maximize along $10^o S$.

4.4. Eddy contribution in ISO

A similar analysis as done in section 3.5 for the west Pacific region is carried out over the Indian ocean to examine the contribution of higher frequency transient eddies such as synoptic disturbances and mesoscale gustiness to the intraseasonal wind speed anomalies (Figure 4.8 , Figure 4.9). Eddy variance in the Indian Ocean locally contributes as much as 20% to the enhancement of the intraseasonal wind speed during the enhanced phases of precipitation for NH summer (phase 4) and SH summer (phase 4). Contributions from eddy variance tend to be largest where precipitation anomalies are larger (see figure 4.4 and figure 4.6). During the southern hemisphere suppressed precipitation phase (Phase 8), the eddy variance contributes 20% to the wind speed anomaly and maximizes in the region of suppressed precipitation, but during the northern hemisphere (Phase 8) summer there is little contribution from eddy variance.

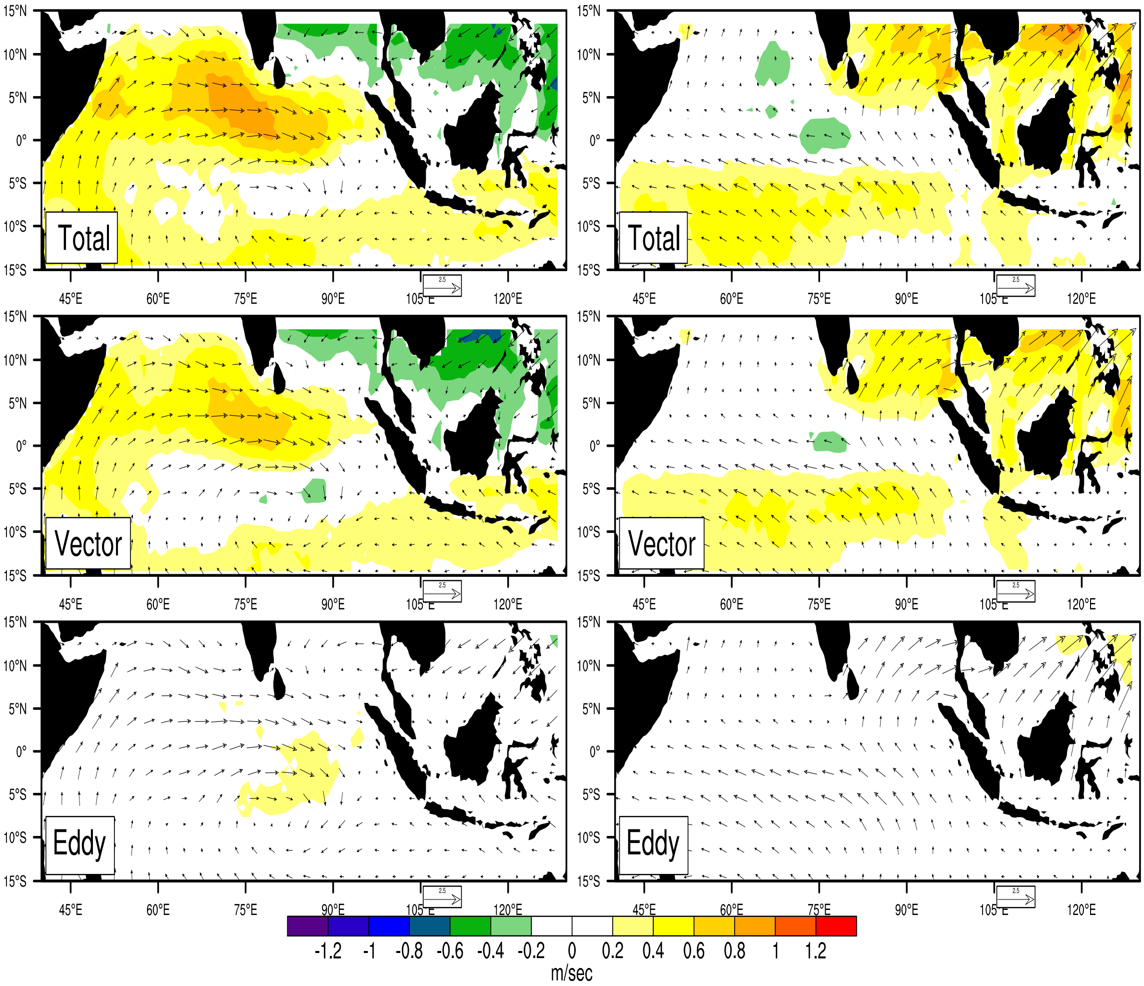

FIGURE 4.8. *Composite of decomposed Intraseasonal wind speed anomalies into Total, Vector and Eddies for the ISO enhanced phase, left panel (Phase 4) and ISO suppressed phase, right panel (Phase 8) during the Northern hemisphere summer. Wind vectors are intraseasonal QuikSCAT wind.*

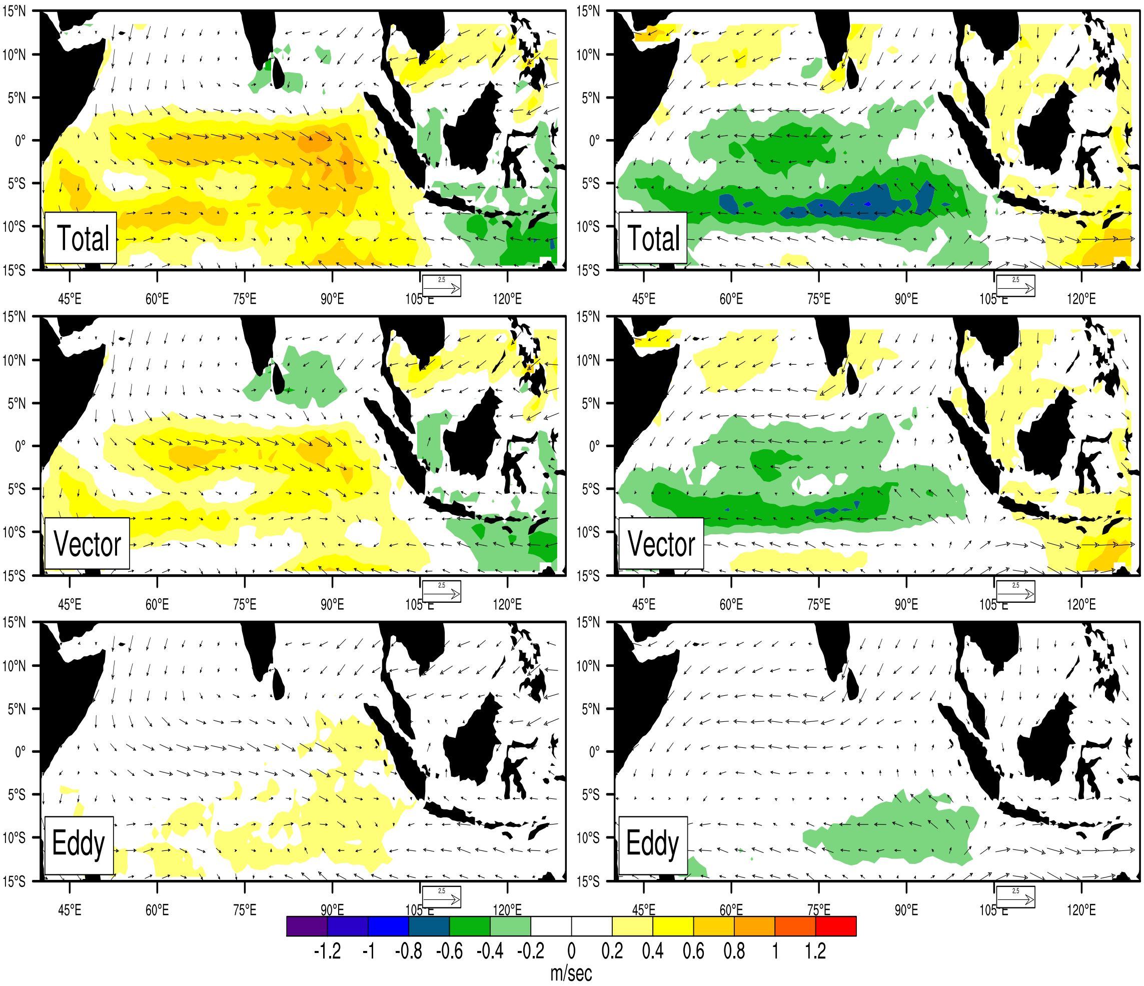

FIGURE 4.9. *Composite of decomposed Intraseasonal wind speed anomalies into Total, Vector and Eddies for the ISO enhanced phase, left panel (Phase 4) and ISO suppressed phase, right panel (Phase 8) during the Southern hemisphere summer. Wind vectors are intraseasonal QuikSCAT wind.*

5. CONCLUSION

This study uses daily averaged satellite precipitation and winds and TAO buoy data during 1998-2005 to document the importance of Wind Induced Surface Heat Exchange (WISHE) to intraseasonal precipitation in the tropical west Pacific and the Indian Ocean. The increase in wind speed during periods of ISO westerly anomalies and enhanced convection implies an increase in the wind-induced component of latent heat flux. Latent heat flux was explicitly computed using TAO buoy data in the tropical west Pacific, and TRMM precipitation was also used to determine the relationship between intraseasonal precipitation and latent heat flux. A significant positive correlation between intraseasonal latent heat flux and precipitation occurs in regions of strong climatological intraseasonal precipitation variance, which suggests that during both SH and NH summer wind-induced surface heat exchange supports intraseasonal convection over the west Pacific. The correlation between intraseasonal latent heat flux and precipitation can be negative in regions outside of those climatologically favored for strong intraseasonal precipitation anomalies. In these regions, anomalies in air-sea humidity difference can provide an important contribution to the latent heat flux anomalies. Also, regions of weak climatological intraseasonal variance feature intraseasonal wind anomalies that are forced remotely, and are thus not strongly coupled to local convection.

The correlation between latent heat flux and precipitation decreases when the latent heat flux is computed using the three day mean vector winds for the buoys, which minimizes mesoscale gustiness and synoptic scale wind variability. This result is consistent with another sensitivity test using QuikSCAT winds and TRMM precipitation in which the correlation between vector wind speed and precipitation decreases when the vector wind is averaged over a $2.5^o \times 2.5^o$ grid, rather than a $1^o \times 1^o$ grid. This implies that higher wavenumber and high frequency features of the flow contribute towards the increase in the wind speed anomalies. A sensitivity study of the various variables involved in the computation of latent heat flux suggests that the latent heat flux is primarily wind driven, and thermodynamic contributions tend to oppose wind-driven components of the latent heat flux anomaly in regions of strong intraseasonal precipitation variability.

The buoy-derived regression coefficient of intraseasonal latent heat flux and precipitation in the west Pacific shows that latent heat flux contributes about 20% of the total intraseasonal precipitation anomaly. The highest regression values are located in regions where the climatological intraseasonal precipitation variance is high. Past work using idealized vertical velocity and moist static energy distributions suggests that this magnitude is approximately sufficient to support a flux-driven convective instability, suggesting that wind-induced surface heat exchange is an important regulator of intraseasonal convection. For a moisture balance dominated by evaporation, precipitation, and moisture convergence, the fact that local evaporation anomalies are only 20% of precipitation indicates that moisture convergence strongly augments the amount of precipitable water available for precipitation on intraseasonal timescales. Thus, a significant forcing by surface fluxes can be amplified through moisture convergence feedbacks (e.g. Bretherton et al. 2004).

Composite QuickSCAT ocean vector winds and the TRMM precipitation show that intraseasonal oscillation (ISO) phases characterized by anomalously westerly flow are associated with an enhancement of convection over the west Pacific and the Indian ocean during both the northern hemisphere summer and the southern hemisphere summer. Periods of ISO easterly anomalies are generally associated with the suppressed convection over the west Pacific and the Indian ocean. Enhancement of wind speed occurs during periods of anomalously westerly flow and enhanced precipitation, and periods of ISO easterly anomalies and suppressed precipitation are associated with negative wind speed anomalies. Wind speed anomalies peak slightly to the southwest of enhanced precipitation anomalies over the Indian ocean during the northern hemisphere summer, and peak wind speed anomalies during the northern hemisphere summer over the west Pacific tend to occur near and to the south of the center of enhanced precipitation anomalies. During southern hemisphere summer, enhanced wind speed is nearly collocated with enhanced precipitation over the west Pacific, in agreement with the ISO structure observed over the west Pacific in other data products (Hendon and Salby 1994, Shinoda et al. 1998). It was also found that in the Indian ocean during the southern hemisphere summer, the wind speed anomalies are reasonably collocated with the enhanced precipitation anomaly. Previous observational results suggest more of a separation between wind speed and precipitation anomalies.

Partioning of the wind-speed reveals that intraseasonal wind speed anomalies have contributions from ISO vector wind anomalies interacting with the climatological flow, and from higher frequency transients such as easterly waves and mesoscale gustiness, smaller scale features that are coupled to convection. The eddy contribution to intraseasonal wind speed anomalies is about 20% in regions of large anomalous precipitation. The ability of climate models to account for such processes may thus negatively impact their simulations of intraseasonal variability.

The ratio of intraseasonal precipitation to evaporation is a good diagnostic against which to test parameterizations of tropical deep convection in climate models. For example, this ratio can be used to examine whether models producing weak intraseasonal variability are characterized by a weak coupling (regression slope) between precipitation and wind-driven latent heat flux. Based on the results derived in this study, it is entirely possible that models exhibiting a weaker coupling between precipitation and latent heat flux may be doing so because they neglect processes such as mesoscale gustiness and other small-scale transients that are often not present in a coarse resolution general circulation model. In future work, I intend to use general circulation model to examine the sensitivity of intraseasonal convective variability to wind-driven surface heat exchange, including sensitivity to mesoscale gustiness. The impact of mesoscale gustiness in climate models can be parameterized in some relatively simple ways (e.g. Redelsbeger et al. (2002)). Further, the full moist static energy budget can be determined in an atmospheric general circulation model in a physically consistent manner, which is often difficult in observations. A modified version of the National Center for Atmospheric Research (NCAR) Community Atmosphere Model (CAM) that exhibits realistic tropical intraseasonal variability will be a possible candidate model (e.g. Maloney and Esbensen 2005).

BIBLIOGRAPHY

[1] Adler, R.F., G.J. Huffman, A. Chang, R. Ferraro, P.P. Xie, J. Janowiak, B. Rudolf, U. Schneider, S. Curtis, D. Bolvin, A. Gruber, J. Susskind, P. Arkin, and E. Nelkin, 2003: The Version-2 Global Precipitation Climatology Project (GPCP) Monthly Precipitation Analysis (1979Present), *J. Hydrometeor.*, 4, 11471167.

[2] Back, L. E., and C. S. Bretherton, 2005: The relationship between wind speed and precipitation in the east Pacific ITCZ, *J. Clim.*, 18, 4317-4328.

[3] Bellon, G., and A. H. Sobel, 2007: Poleward-propagating intraseasonal monsoon disturbances in an intermediate-complexity axisymmetric model, *J. Atmos. Sci.*, in press

[4] Bergman, J. W., H. H. Hendon, and K. M. Weickmann, 2001: Intraseasonal air-sea interactions at the onset of El Nino, *J. Clim.*,14,1702-1719.

[5] Bony, S., and K. A. Emanuel, 2005: On the role of moist processes in Tropical Intraseasonal variability : Cloud-Radiation and Moisture-Convection feedbacks, *J. Atmos. Sci.*, 62, 2770-2789.

[6] Bretherton, C.S., M.E. Peters, and L.E. Back, 2004: Relationships between Water Vapor Path and Precipitation over the Tropical Oceans, *J. Climate*, 17, 15171528.

[7] Chang, C. P., 1977: Viscous internal gravity waves and low-frequency oscillations in the tropics, *J. Atmos. Sci.*, 34,901-910.

[8] Chang, C. P., and H. Lim, 1988: Kelvin-wave CISK: a possible mechanism for the 20-50 day oscillation, *J. Atmos. Sci.*,45,1709-1720.

[9] Chelton, D. B., and M. H. Freilich, 2005: Scatterometer-based assessment of 10-m wind analyses from the operational ECMWF and NCEP numerical weather prediction models, *Mon Wea. Rev.*, 133, 409-429.

[10] Crum, F. X., and T. J. Dunkerton, 1992: Analytic and Numerical Models of Wave-CISK with Conditional Heating, *J. Atmos. Sci.* ,49,1693-1708

[11] Emanuel, K. A., 1987: An air-sea interaction model of intraseasonal oscillations in the tropics, *J. Atmos. Sci.*, 44, 2324–2340

[12] Emanuel, K. A., 1988: Reply, *J. Atmos. Sci.*, 45, 3528–3530

[13] Esbensen, S. K., and M. J. McPhaden, 1996: Enhancement of tropical ocean evaporative and sensible heat flux by atmospheric mesoscale systems, *J. Clim.*, 9, 2307–2325

[14] Fairall, C. W., E. F. Bradley, J. E. Hare, A. A. Grachev, and J. B. Edson (2003): Bulk parameterization of air-sea fluxes: Updates and verification for the COARE algorithm, *J. Clim.*, 16, 571-591.

[15] Gill, A. E., 1980: Some simple solutions for heat-induced tropical circulation, *Quart. J. Roy. Meteor. Soc.*,106, 447-462

[16] Gutzler, D. S., and R. A. Madden, 1989: Seasonal variations in the structure of intraseasonal tropical wind fluctuations, *J. Atmos. Sci., 46, 641-660*,46,641-660.

[17] Hayes, S. P., L. J. Mangum, J. Picaut, A. Sumi, and K. Takeuchi, 1991: TOGA-TAO: A moored array for real-time measurements in the tropical Pacific Ocean, *Bull. Amer. Meteor. Soc.*,72, 339-347.

[18] Hayashi, Y. Y., and A. Sumi, 1986: The 30-40 day oscillation simulated in an 'Aqua Planet' model, *J. Meteor. Soc. Japan*,64,451-467

[19] Hendon, H. H., and J. Glick, 1997: Intraseasonal Air-Sea interaction in the Tropical Indian and Pacific Oceans, *J. Clim.*,10, 647-661.

[20] Hendon, H. H., and B. Liebmann, 1990: The intraseasonal (30-50 day) oscillation of the Australian summer monsoon, *J. Atmos. Sci.*,47,2909-2923.

[21] Hendon, H. H., and M. L. Salby, 1994: The life cycle of the Madden-Julian oscillation, *J. Atmos. Sci.*,51, 2225-2237.

[22] Hendon, H. H., and M. L. Salby, 1996: Planetary-Scale Circulation forced by Intraseasonal Variations of observed convection, *J. Atmos. Sci.*,53,1751-1758.

[23] Higgins, R. W., and K. C. Mo, 1997: Persistent North Pacific circulation anomalies and the tropical intraseasonal oscillation, *J. Clim.*,10,223244.

[24] Higgins, R. W., J. K. E. Schemm, W. Shi, and A. Leetmaa, 2000: Extreme Precipitation events in the Western United States related to Tropical forcing, *J. Clim.*,13,793-820.

[25] Jones, C. and B. C. Weare (1996): The role of low-level moisture convergence and ocean latent heat fluxes in the Madden-Julian Oscillation: An observational analysis using ISCCP data and ECMWF analyses, *J. Clim.*, 11, 1057-1072.

[26] Kessler, W. S., M. J. McPhaden, and K. M. Weickmann, 1995: Forcing of Intraseasonal Kelvin waves in the equatorial Pacific, *J. Geophys. Res.*,100,10613-10631.

[27] Kiladis, G. N., K. H. Straub, and P. T. Haertel, 2005: Zonal and vertical structure of the MaddenJulian oscillation, *J. Atmos. Sci.*, 62, 27902809.

[28] Kummerow, C., J. Simpson, O. Thiele, W. Barnes, A.T.C. Chang, E. Stocker, R.F. Adler, A. Hou, R. Kakar, F. Wentz, P. Ashcroft, T. Kozu, Y. Hong, K. Okamoto, T. Iguchi, H. Kuroiwa, E. Im, Z. Haddad, G. Huffman, B. Ferrier, W.S. Olson, E. Zipser, E.A. Smith, T.T. Wilheit, G. North, T. Krishnamurti, and K. Nakamura, 2000: The Status of the Tropical Rainfall Measuring Mission (TRMM) after Two Years in Orbit, *J. Appl. Meteor.*, 39, 19651982.

[29] Lau, K. M., and P. H. Chan, 1986: Aspects of the 40-50 day oscillation during the northern summer as inferred from outgoing longwave radiation, *Mon. Wea. Rev.*, 114, 13541367.

[30] Lau, K. M., and L. Peng, 1987: Origin of low-frequency (Intraseasonal) oscillations in the Tropical Atmosphere. Part I: Basic Theory, *J. Atmos. Sci.*, 44, 950-972.

[31] Lau, K. M., and T. J. Philips, 1986: Coherent Fluctuations of Extratropical Geopotential Height and Tropical Convection in Intraseasonal Time scale, *J. Atmos. Sci.*,43,1164-1181.

[32] Lau, K. M., and C. H. Sui, 1997: Mechanism of Short-Term Sea Surface Temperature Regulation: Observations during TOGA COARE, *J. Clim.*, 10,465472.

[33] Lawrence, D. M., and P. J. Webster, 2002: The Boreal Summer Intraseasonal Oscillation: Relationship between Northward and Eastward Movement of Convection, *J. Atmos. Sci.* , 59, 1593-1606.

[34] Lee, M., I. Kang, J. Kim, and B. E. Mapes, 2001: Influence of cloud-radiation interaction on simulating tropical intraseasonal oscillation with an atmospheric general circulation model, *J. Geophys. Res.*,106,14219-14233.

[35] Liebmann, B., H. Hendon and J. Glick, 1994: The relationship between tropical cyclones of the western Pacific and Indian oceans and the Madden-Julian Oscillation, *J. Meteorol. Soc. Jpn.*,72,401-411.

[36] Lim, H., T. K. Lim, and C. P. Chang, 1990: Reexamination of wave-CISK theory: Existence and propoerties of nonlinear wave-CISK modes, *J. Atmos. Sci.*, 47, 3078-3091.

[37] Lin, J., and B. E. Mapes, 2004: Radiation Budget of the Tropical Intraseasonal Oscillation, *J. Atmos. Sci.* , 61, 2050-2062.

[38] Lindzen, R. S., 1974: Wave-CISK in the tropic, *J. Atmos. Sci.* ,31,156-179.

[39] Madden, R.A., and P. R. Julian, 1971: Detection of a 40-50 day oscillation in the zonal wind in the tropical Pacific, *J. Atmos. Sci.*,28,702-708.

[40] Madden, R.A., and P. R. Julian, 1972: Description of global-scale circulation cells in the tropics with a 40-50 day period, *J. Atmos. Sci.*,29,1109-1123.

[41] Madden, R. A., 1986: Seasonal variations of the 40-50 day Oscillation in the Tropics, *J. Atmos. Sci.*,43,3138-3158.

[42] Madden, R.A., and P. R. Julian, 1994: Observation of the 40-50 day tropical oscilation - A review, *Mon. Wea. Rev.*,122,814-837.

[43] Maloney, E. D., D. B. Chelton, and S. K. Esbensen, 2007: Subseasonal SST Variability in the Tropical Eastern North Pacific During Boreal Summer, *J. Climate*, accepted pending major revisions.

[44] Maloney, E. D., and M. J. Dickinson, 2003: The Intraseasonal Oscillation and the Energetics of Summertime Tropical Western North Pacific Synoptic-Scale Disturbances, *J. Atmos. Sci.*,60,2153-2168.

[45] Maloney, E. D., and S. K. Esbensen, 2003: The Amplification of East Pacific Madden-Julian Oscillation Convection and Wind Anomalies during June-November, *J. of Clim.*,16,3482-3497.

[46] Maloney, E. D., and S. K. Esbensen, 2005: A Modeling Study of Summertime East Pacific Wind-Induced Ocean-Atmosphere Exchange in the Intraseasonal Oscillation, *J. of Clim.*,18,568-584.

[47] Maloney, E. D., and S. K. Esbensen, 2007: Satellite and Buoy Observations of Boreal Summer Intraseasonal Variability in the Tropical Northeast Pacific, *Mon. Wea. Rev.*,135,3-19.

[48] Maloney, E. D., and D. L. Hartmann, 1998: Frictional Moisture Convergence in a Composite Life Cycle of the Madden-Julian Oscillation, *J. Climate.*,11,2387-2403.

[49] Maloney, E.D., and J. T. Kiehl, 2002: MJO-Related SST Variations over the Tropical Pacific during Northern Hemisphere Summer, *Mon. Wea. Rev.*,122,814-837.

[50] Maloney, E. D., and A. H. Sobel, 2004: Surface fluxes and Ocean Coupling in the Tropical Intraseasonal Oscillation, *J. Clim.* ,17,4368-4386.

[51] Mapes, B. E., 2000: Convective inhibition, subgridscale triggering and stratiform instability in a toy tropical wave model, *J. Atmos. Sci.*,57,1515-1535.

[52] McPhaden, M. J., 1995: The Tropical Atmosphere Ocean array is completed, *Bull. Amer. Meteor. Soc.*,76, 739-741.

[53] Moskowitz, B. M., and C. S. Bretherton, 2000: An analysis of frictional feedback on a moist equatorial Kelvin mode, *J. Atmos. Sci.*, 57, 21882206.

[54] Namaguti, A., and Y. Y. Hayashi, 1991: Behaviour of the cumulus activity and the structures of the circulations in the 'Aqua-planet' model. Part II: Large-scale structures and evaporations-wind feedback, *J. Meteor. Soc. Japan*,69,563-579.

[55] Neelin, J. D., I. M. Held, and K. H. Cook, 1987: Evaporation-wind feedback and low frequency variability in the tropical atmosphere, *J. Atmos. Sci.*,44,2341-2348.

[56] Raymond, D. J., 2001: A new model of the Madden-Julian Oscillation, *J. Atmos. Sci.*,58,2807-2819.

[57] Redelsperger, J., -L, F. Guichard, and S. Mondon, 2000: A parameterization of mesoscale enhancement of suface fluxes for large-scale models, *J. Clim.*,13,402-421

[58] Salby, M.L., and H. H. Hendon, 1994: Intraseasonal behaviour of clouds, temperature, and motion in the Tropics, *J. Atmos. Sci.*,51,2207-2224.

[59] Sui, H. S., and K. M. Lau, 1989: Origin of low-frequency (Intraseasonal) oscillations in the Tropical Atmosphere. Part II: Structure and propagation of mobile Wave-CISK modes and their modeification by lower boundary forcings, *J. Atmos. Sci.*, 46, 37-56.

[60] Shinoda, T., H. H. Hendon, and J. Glick, 1998: Intraseasonal variability of surface fluxes and sea surface temperature in the tropical Indian and Pacific Oceans, *J. Atmos. Sci.*,11,1685-1702.

[61] Slingo, J. M., et al. 1996: Intraseasonal oscillation in 15 Atmospheric General Circulation Models: Results from a AMIP diagnostic subproject, *Clim. Dyn.*,12,325-357.

[62] Sperber, K. R. (2003): Propagation and vertical structure of the Madden-Julian Oscillations, *Mon. Wea. Rev.*, 131, 3018-3037.

[63] Takayabu, Y. N., T. Iguchi, M. Kachi, A. Shibata, and H. Kanzawa, 1999: Abrupt termination of the 1997-98 El Nino in response to a Madden-Julian Oscillation, *Nature*,402,279-282.

[64] Wang, B., 1998a: Dynamics of Tropical Low-Frequency Waves : An Analysis of the Moist Kelvin Wave, *J. Atmos. Sci.*, 45, 2051-2065.

[65] Wang, B., and H. Rui, 1990a: Dynamics of the coupled moist Kelvin-Rossby wave on an equatorial beta plane, *J. Atmos. Sci.*, 47, 397-413.

[66] Wang, B., and H. Rui, 1990b: Synoptic climatology of transient tropical intraseasonal convective anomalies : 1975-1985, *Meteorol. Atmos. Phys.*, 44, 43-61.

[67] Wang, B. and T. Li 1994: Convective interaction with boudary-layer dynamics in the development of a tropical intraseasonal system, *J. Atmos. Sci.* 51,1386-1400.

[68] Wheeler, M., and H. H. Hendon, 2004: An all season real-time multivariate MJO index: Development of an index for monitoring and prediction, *Mon. Wea. Rev.*, 132,1917-1932.

[69] Wheeler, M., and G. N. Kiladis, 1999: Convectively coupled equatorial waves: Analysis of clouds and temperature in the wave, *J. Atmos. Sci.*,29,1109-1123.

[70] Winkler, C. R., M. Newman, and P. D. Sardeshmukh, 2001: A Linear Model of Wintertime Low-Frequency Variability. Part I: Formulation and Forecast Skill, *J. Clim.*,14,4474-4494.

[71] Xie, S. P., A. Kubokawa, and K. Hanawa (1993a): Evaporation-wind feedback and the organizing of tropical convection on the planetray scale. Part I : Quasi-Linear Instability, *J. Atmos. Sci.* ,50,3873-3883.

[72] Xie, S. P., A. Kubokawa, and K. Hanawa (1993b): Evaporation-wind feedback and the organizing of tropical convection on the planetray scale. Part II : Nonlinear evolution, *J. Atmos. Sci.* ,50,3884-3893.

[73] Xu, K. M., and K. A. Emanuel, 1989: Is the tropical atmosphere conditionally unstable?, *Mon. Wea. Rev.*,117,1471-1479.

[74] Yasunari, T., 1979: Cloudiness fluctuations associated with the Northern Hemisphere summer monsoons, *J. Meteorol. Soc. Jpn.*,57,227-242.

[75] Yu, J.-Y., C. Chou, and J. D. Neelin, 1998: Estimating the gross moist stability of the tropical atmosphere, *J. Atmos. Sci.*, 55, 1354-1372.

[76] Zhang, C., 1996: Atmospheric intraseasonal variability at the surface in the western Pacific Ocean, *J. Atmos. Sci.*,53,739-758.

[77] Zhang, C., and M. Dong (2004): Seasonality of Madden Julian Oscillation, *J. Clim.*,17,3169-3180.

[78] Zhang, G. J., and M. J. McPhaden (1995): The Relationship between Sea Surface Temperature and Latent Heat Flux in the Equatorial Pacific, *J. Clim.* , 8, 589-605.

[79] Zhang, G. J., and M. J. McPhaden (2000): Intraseasonal Surface Cooling in the Equatorial Western Pacific, *J. Clim.* , 13, 2261-2276.

[80] Zhang, C., 2005: Madden-Julian Oscillation, Rev. Geophys., 43, RG2003